Journal of the European Ceramic Society 46 (2026) 118595

Contents lists available at ScienceDirect

Journal of the European Ceramic Society

journal homepage: www.elsevier.com/locate/jeurceramsoc

Wollastonite-derived 316L-$CaTiSiO_5$ core-shell scaffolds for bone substitutes: Mechanical properties and in-vitro study

Vanessa Gastaldi [a], Devis Bellucci [b,*], Alessia Mazzilli [c], Federica Boraldi [c], Valeria Cannillo [b,*], Lisa Biasetto [a]

[a] *Department of Industrial Engineering, University of Padova, Via Marzolo 9, Padova 35131, Italy*
[b] *Department of Engineering "Enzo Ferrari", University of Modena and Reggio Emilia, Via P. Vivarelli 10, Modena 41125, Italy*
[c] *Department of Life Sciences, University of Modena and Reggio Emilia, Modena 41125, Italy*

ARTICLE INFO

Keywords:
Co-extrusion
Direct Ink Writing
Scaffolds
Bone tissue engineering
Sphene

ABSTRACT

In this work, co-extrusion Direct Ink Writing 3D printing technology was used to produce 316L-sphene ($CaTiSiO_5$) core-shell scaffolds, with the main objective of developing a new generation of bone substitutes capable of mimicking the mechanical behavior of natural bone under compressive load. The presence of a ductile core in the struts of bioceramics scaffolds increases the strain energy density, preventing brittle fracture and enabling a more graceful failure. The proposed CO_2-free synthesis route for sphene, without decomposition byproducts, preserves the intrinsic ductility of the stainless-steel core while maintaining a level of porosity suitable for promoting the bioactive properties of the bioceramic shell. Compression tests on the 3D-printed bio-scaffolds demonstrated that the incorporation of a ductile metallic core alters the fracture behavior under compressive loading, resulting in a fourfold increase in strain energy density compared with fully ceramic scaffolds, while preserving a high porosity (~70%). The in-vitro studies confirmed the bioactive behavior of both sphene and 316L–sphene scaffolds, as evidenced by the formation of calcium phosphate phases and apatite-like precipitates after immersion in SBF. ICP-MS analyses revealed very low metal ion release (Fe $<$ 0.3 ppm; Ti $<$ 20 ppb; Cr $<$ 10 ppb; Ni $<$ 5 ppb; Mn $<$ 100 ppb). Cytotoxicity tests showed cell viability consistently above the 70% threshold defined by ISO 10993–5, confirming the absence of cytotoxic effects. These results represent a first step toward the development of a new generation of composite bio-scaffolds, in which the combination of materials with both structural and functional properties may enable the fabrication of patient-specific implants. Further studies will require the optimization of the core-shell interface strength, the study of their mechanical behavior under dynamic loading conditions, and the assessment of the effect of scaffold architecture on their bioactive response.

1. Introduction

The use of 3D printing technologies for the fabrication of bioceramic scaffolds as bone substitutes is gaining increasing interest, owing to their ability to enhance bioactivity through topology optimization and to enable the production of patient-specific implant geometries. Vat Polymerization Techniques, VP (i.e. Sterolitography Apparatus-SLA, Digital Laser Processing-DLP) and Materials Extrusion Technologies, MEX (i.e. Direct Ink Writing-DIW, Fused Deposition Modeling-FDM) are frequently employed for shaping optimized geometries with novel glass and ceramic materials, thus leveraging the potential of a new generation of bioglasses and bioceramics [1,2]. DIW and DLP are among the most widely employed technologies for the fabrication of scaffolds intended for bone substitution. The literature extensively reports on bioceramics- and bioglasses-based lattice structures, particularly regarding their fabrication routes and mechanical and functional characterization. Porosity, permeability and mechanical strength under compression load are the most widely engineered properties, since they represent the necessary prerequisites to mimic natural bone interaction with body fluids and under load service. Commonly used bioceramics include hydroxyapatite (HA), tricalcium phosphate (TCP) [3], zirconia [4], and silicates [5]. In Table 1 the most recent literature of bioceramics and bioglasses based scaffolds fabricated by DIW and DLP are reported.

In [7], HA scaffolds were 3D printed by DIW, possessing struts with porosity that was tuned by the formulation of an emulsion ink. In [10], the optimization of printing parameters to fabricate β-TCP scaffolds by

---

* Corresponding authors.
E-mail addresses: devis.bellucci@unimore.it (D. Bellucci), valeria.cannillo@unimore.it (V. Cannillo).

https://doi.org/10.1016/j.jeurceramsoc.2026.118595
Received 23 January 2026; Received in revised form 4 June 2026; Accepted 7 June 2026

Table 1
Printing technology, total porosity, compressive strength of bioceramics and bioglasses based scaffolds.

Material	Printing technology	Porosity [%]	Compressive strength [MPa]	Ref
HA	DIW	67.8 ± 2.9	3.8 ± 1.0	[6,7]
		73.7 ± 0.5	3.5 ± 0.6	
	DLP	60	3.3 ± 0.3	[8,9]
		80 ± 2	1.6 ± 0.8	
β-TCP	DIW	60	2.6 ± 0.1	[10]
	DLP	73.5 ± 0.05	1.4 ± 0.2	[11]
	DLP	65	1.3 ± 0.2	[12]
		75	0.7 ± 0.1	
HA/ β-TCP (50–50 wt%)	DIW	72.4 ± 2.1	3.6 ± 0.6	[13]
$CaSiO_3$	DIW	65	3.6 ± 0.1	[14]
Sphene $CaTiSiO_5$	DIW	65 ± 1	9.3 ± 2.2	[15, 16]
		75 ± 1	4.0 ± 0.8	
Bioglass 45S5	DIW	74 ± 2	5.0 ± 1.0	[17]
	DLP	> 70	1.7 ± 0.1	[18]
Sr-doped 13–93 glass	DLP	63	5.8 ± 0.6	[19]

DIW was investigated, reaching a good control on the imparted design porosity (60%, 80% and 100%). To tune the degradation rate of lattices, several studies propose the combination of HA and β-TCP to combine HA chemical stability with β-TCP high resorbability, as reported in [13]. Other works investigate the fabrication of sphene ($CaTiSiO_5$) scaffolds by DIW, as shown in [15] and [16], where the effect of topology on mechanical performances and permeability is investigated, finding good matches with the requirements for biomedical purpose. Most common bioactive glasses, such as 45S5, 13–93 and their doped equivalents, are frequently used to fabricate bone substitutes thanks to their excellent bioactivity and biodegradability [20]. In [18], structures with different and highly porous designs were fabricated, showing a compressive strength of 1.7 MPa and a verified bioactivity thanks to the rapid ion release. Available examples also include the production of strontium-doped 13–93 Bioglass scaffolds by DLP [19], which exhibited compressive strength (5.8 MPa), porosity (~63%) and permeability (0.97×10^{-8} m^2) values comparable to those of cancellous bone.

Despite the bioactive properties bioceramics and bioglasses offer, their intrinsic brittleness limits their applications to substitution of non-loading damaged bone of limited size. For dynamic load bearing applications, metallic alloys (such as Ti6Al4V and 316L) represent the most conservative choice offering biocompatibility and good structural integrity over time. However, metals' excellent mechanical properties, being significantly higher than those of natural bone, can lead to inadequate stresses on the surrounding bone tissue causing its absorption (stress shielding) [21]. In this context, 3D-printing technologies enable improved performance of metallic implants by introducing controlled structural porosity, which enhances integration with bone tissue and yields mechanical properties closer to those of native bone, thereby mitigating the onset of stress shielding [22]. However, the release of metal ions into the body can increase toxicity levels, thereby compromising cell health [23]. Consequently, the use of composite materials is particularly appealing, as it makes possible to overcome the limitations associated with the intrinsic brittleness of bioceramics and bioactive glasses.

Thanks to its versatility, DIW represents a technology well suited for the fabrication of composite architectures. Attempts in the fabrication of composite structures for bone substitutes include DIW-printed porous ceramic scaffolds infiltrated with polymers [24], which help tailor their mechanical properties to resemble those of native bone. Another approach involves ceramic matrix composites, as shown in [25], where bioactive silicate (13−93) glass-based scaffolds were fabricated with Ti fibers as reinforcement, thanks to which an increase in toughness (70%) and flexural strength (40%) was observed. Moreover, co-axial DIW represents a promising approach for fabricating core–shell structures for biomedical applications as well as for sensors, electronic devices, batteries, and automotive components [26,27]. Several approaches for implementing the co-extrusion process have been reported in the literature. The co-extrusion system adopted in the present study, previously reported in [28], consists of two detachable concentric conical channels specifically designed to facilitate ink flow. Unlike the configuration described in [29], characterized by perpendicular cylindrical channels, the present set-up employs conical channels intersecting at approximately 45°, while, differently from the approach proposed in [30], the core–shell architecture is generated directly during the extrusion process rather than being predefined within the syringe.

The use of nozzles with concentric channels can be exploited to fabricate lattices made of hollow struts, as reported in [31]. $Ca_7Si_2P_2O_{16}$-based scaffolds with multi-oriented hollow channels, exhibiting a compressive strength of up to 5 MPa, improve cell adhesion and promote new bone formation, demonstrating their suitability for non-load-bearing bone substitutes. In [29], the enhancement of the mechanical properties of porous alumina-based structures by co-extruding a dense core with an outer porous shell is investigated. The results indicate that compressive strength is significantly improved in components with porosity below 30%, while at higher porosity the contribution of the dense core is not evident. In [28,30], steel core and alumina shell were co-extruded, highlighting the effect of core-shell interface adhesion and core over shell diameter ratio on the mechanical response of the produced composites.

This research group recently reported on the production of 316L-$CaTiSiO_5$ (sphene) core-shell scaffolds by co-extrusion DIW technologies, where the ductile 316L core offers a mechanical support without directly interacting with body fluids (thanks to the bioactive shell), thus enhancing bioactivity, preventing dissolution of alloying elements and improving load bearing functionality [32]. $CaTiSiO_5$ is a calcium titanate silicate exhibiting good chemical stability and well-established biocompatibility, as demonstrated by both in vitro and in vivo studies [33,34]. Sphene interaction with cells favors their adhesion and proliferation, thereby proving its suitability for biomedical applications. In our previous work, we showed good control of the 3D printing technology; however, the synthesis route for sphene production led to severe oxidation of the 316 L core, due to the CO_2 generated during the synthesis of sphene. In this work, we propose a CO_2-free approach for the synthesis of sphene starting from $CaSiO_3$ and TiO_2 precursors, with the aim of preserving the 316L ductility without compromising the shell bioactivity. The effect of the proposed synthesis route was studied in terms of microstructural, mechanical, and in-vitro biological properties on full and core-shell scaffolds. In particular, the bioactivity of the fabricated samples was evaluated *in vitro* in Simulated Body Fluid (SBF) [35], and the ionic release from the materials was monitored over time. Moreover, the cytotoxicity of the scaffolds was successfully assessed on murine fibroblast cultures in accordance with the ISO 10993–5 and 10993–12 guidelines.

2. Materials and methods

The choice of using 316L as the core material for the bio-scaffolds produced in this work was driven by the results of preliminary tests performed on the well accepted Ti6Al4V. Due to the high reactivity of this Ti alloy toward oxygen and carbon, severe embrittlement was observed after sintering and co-sintering with $CaTiSiO_5$ using the available experimental set-up. Nevertheless, potential issues related to nickel ion release and long-term biocompatibility should be carefully considered when employing 316L stainless steel in biomedical composite structures. In this regard, preliminary cytotoxicity tests were performed on the developed composite scaffolds, and the corresponding results are reported in the dedicated results section. Furthermore, ion-release tests were also conducted to specifically assess nickel release and to exclude the possibility that the samples released this element in significant amounts.

2.1. Inks formulation

2.1.1. 316L ink

The gas-atomized 316L powders ($d_{10} < 4.1$ μm, $d_{50} < 6.8$ μm, $d_{90} < 10.2$ μm) were purchased from Metalpine GmbH (Graz, Austria). A polymeric water-based binder was prepared by dissolving polyvinyl alcohol (PVA) (Mw = 9000–10.000 $g \cdot mol^{-1}$, 80% hydrolyzed, Sigma-Aldrich, Steinheim, Germany, named as PVA_{LMW}, Low Molecular Weight PVA) and polyethylene glycol (PEG) (Mn = 950–1000 $g \cdot mol^{-1}$, Sigma-Aldrich, Steinheim, Germany) in distilled water, using the following weight ratios: PVA_{LMW}:PEG:H_2O = 18.75:16.25:65. The metallic powders were mixed with the binder and a poly(ethyleneimine) (PEI) solution (Mn = 1800 $g \cdot mol^{-1}$, 50 wt% in H_2O, Sigma-Aldrich, Steinheim, Germany), added at 1 wt% with respect to the total powder weight, following the same procedure previously described in [32]. The composition of the optimized ink is reported in Table 2.

2.1.2. Sphene ink

Wollastonite powders ($CaSiO_3$, kindly supplied by Silca Italia Srl, Scorzè, Venice, Italy) were ground in a ball mill using an agate jar and distilled water (31.4 wt% $CaSiO_3$, 68.6 wt% H_2O). Milling was performed in six cycles of 15 min each at 400 rpm. The resulting slurry was dried overnight at 60 °C to ensure complete water evaporation, after which the powders were manually ground with a mortar. The final particle size distribution, measured using a laser granulometer (Mastersizer 2000, Malvern Panalytical, Worcestershire, UK), was characterized by $d_{10} < 2.6$ μm, $d_{50} < 11.1$ μm, $d_{90} < 34.8$ μm.

The $CaSiO_3$ powders were subsequently blended with TiO_2 nanopowders (anatase phase, $d_{99} < 330.5$ nm, Inframat Advanced Materials, Manchester, CT 06042 USA) in a centrifugal mixer (Hauschild Speedmixer) operated for 5 min at 300 rpm. The precursor powders were weighed to obtain a 1:1 molar ratio between $CaSiO_3$ and TiO_2, thus ensuring the proper synthesis of sphene ($CaTiSiO_5$) during the thermal treatment. The ink formulation was prepared by dispersing the mixed powders in a polymeric binder, with the addition of PEI at 1 wt% relative to the total powder mass, and glycerol (Prolabo, Fontenay-sous-Bois, France) at 3.5 wt% relative to the total powder mass. The polymeric binder possessed the same composition as the one described above for 316L ink, except for the type of PVA used. Specifically, 25 wt% of the total PVA (Sigma-Aldrich, Steinheim, Germany) had a molecular weight (Mn) of 85000–124000 $g \cdot mol^{-1}$ (denoted as PVA_{HMW}, HMW, High Molecular Weight PVA), whereas the remaining 75 wt% corresponded to PVA_{LMW}, as defined in 2.1.1. Powders were incorporated through four successive additions, each followed by mixing in a Thinky mixer for 2 min at 2000 rpm. The viscosity of the ink was adjusted by adding distilled water at 5.5 wt% relative to the total powder content. The prepared ink was then transferred to a syringe and subjected to a defoaming step in the Thinky mixer for 4 min at 2200 rpm. The final composition of the ink, expressed in weight percentages, is reported in Table 3.

2.2. Rheological characterization of the inks

Rheological analyses were conducted on the formulated inks to identify the parameters relevant for assessing their suitability for DIW printing. Optimization of the co-extrusion process requires accurate control of the flow behavior of both inks to maintain the continuity of the inner core while providing an outer shell capable of preserving the shape and preventing structural collapse. Measurements were performed using a plate–plate rheometer (d = 40 mm, Netzsch, Kinexus, Selb, Germany), with distilled water used as the solvent trap. Amplitude sweep tests in stress-controlled mode were performed to evaluate the variation of the storage (G′) and loss (G″) moduli as a function of applied shear stress. The yield stress was determined as the stress corresponding to 95% of G′, while the crossover stress was identified at the intersection of G′ and G″. The applied shear stress ranges varied depending on the ink: from 0.1 Pa to 100 Pa for the 316L steel-based ink, and from 1 Pa to 5000 Pa for the $CaTiSiO_5$-based ink. The frequency was set at 0.5 Hz. Thixotropy measurements were then carried out to determine the recovery time of the mixtures. The test consisted of three phases: (i) 30 s at 0.1 Pa, (ii) 30 s at 100 Pa, and (iii) 600 s at 0.1 Pa. During the first phase, the mixture, subjected to a small stress (0.1 Pa), exhibited a solid-like viscosity; under higher stress (100 Pa), the ink flows like a liquid, showing low viscosity. When a lower stress (0.1 Pa) is applied again, the structure starts to rebuild; the time required to recover the initial viscosity was defined as the recovery time.

Table 2
316L ink composition expressed in terms of weight percentages.

	[wt %]	PVA_{LMW} [wt %]	PEG [wt %]	H_2O [wt %]	PEI [wt %]
316L ink	90.7	1.6	1.4	5.4	0.9

Additional information regarding the rheological characterization of the inks is provided in Section S1 of the Supplementary Information.

2.3. 3D-printing of core-shell structures

The co-extrusion of the inks was performed using a WASP 2040 Clay printer (WASP, Massa Lombarda-Ravenna, Italy) equipped with a custom-designed core–shell nozzle consisting of two concentric channels with a conical geometry. The inks were extruded through the nozzle under pressure, which varied depending on the mixture and the channel through which it flowed. The core ink was formulated to allow modulation of the extrusion as a function of the applied printing pressure, thereby enabling control over the size of the metallic core. In this case, a pressure of 0.5 MPa was used to maximize the volume occupied by the steel filament. For the shell ink, which must provide structural support and prevent collapse of the core during printing, extrusion was carried out by applying a minimum pressure of 0.45–0.5 MPa. The fabricated geometries included filaments and scaffolds composed of solid, shell, and core–shell struts. Sphene-based and composite filaments were produced by extruding the inks through the nozzle and cutting them once the desired length was reached (~30 mm), then avoiding the flattening effect due to adhesion to the printing surface. 316L solid filaments were instead printed as a grid, since free extrusion from the nozzle was not feasible due to collapse under their own weight. This grid configuration also allowed to avoid bending during sintering. An overview of the produced structures, and their corresponding dimensions and printing parameters is reported in Fig. 1.

2.4. Thermal debinding and sintering

Preliminary studies on $CaSiO_3$ and TiO_2 reactivity toward sphene formation were performed on a.r. powders and reported on Section S2 of the Supplementary Information. Thermal treatment was selected based on the results of thermogravimetric and differential thermal analyses (TGA-DTA differential scanning calorimetry 3 star System, Mettler Toledo, Milano, Italy) conducted on small drops of dried inks (10 °C/min under Argon up to 1400 °C). The heating profile consisted of a ramp at 1 $°C \cdot min^{-1}$ from room temperature to 550 °C, followed by a 1 h dwell at 550 °C to ensure complete removal of the organic content. The temperature was then increased at a rate of 1 $°C \cdot min^{-1}$ up to the maximum sintering temperature of 1240 °C, which was maintained for 1 h. The cooling phase was performed at a rate of 3 $°C \cdot min^{-1}$ down to 250 °C and then continued naturally to room temperature. Oxygen content in the sintering atmosphere was not monitored. Although 1300 °C is considered optimal for sphene synthesis [16] (more details available in section S2 of the Supplementary Information), co-sintering with steel requires a compromise, since higher temperatures may promote steel oxidation, whereas lower temperatures can result in incomplete sphene formation

Table 3
$CaTiSiO_5$ ink composition expressed in terms of weight percentages.

	$CaSiO_3$ [wt%]	TiO_2 [wt%]	PVA_{LMW} [wt%]	PVA_{HMW} [wt%]	PEG [wt%]	H_2O [wt%]	PEI [wt%]	Glycerol [wt%]
$CaTiSiO_5$ ink	40.1	27.5	3.6	1.2	4.2	20.4	0.7	3.7

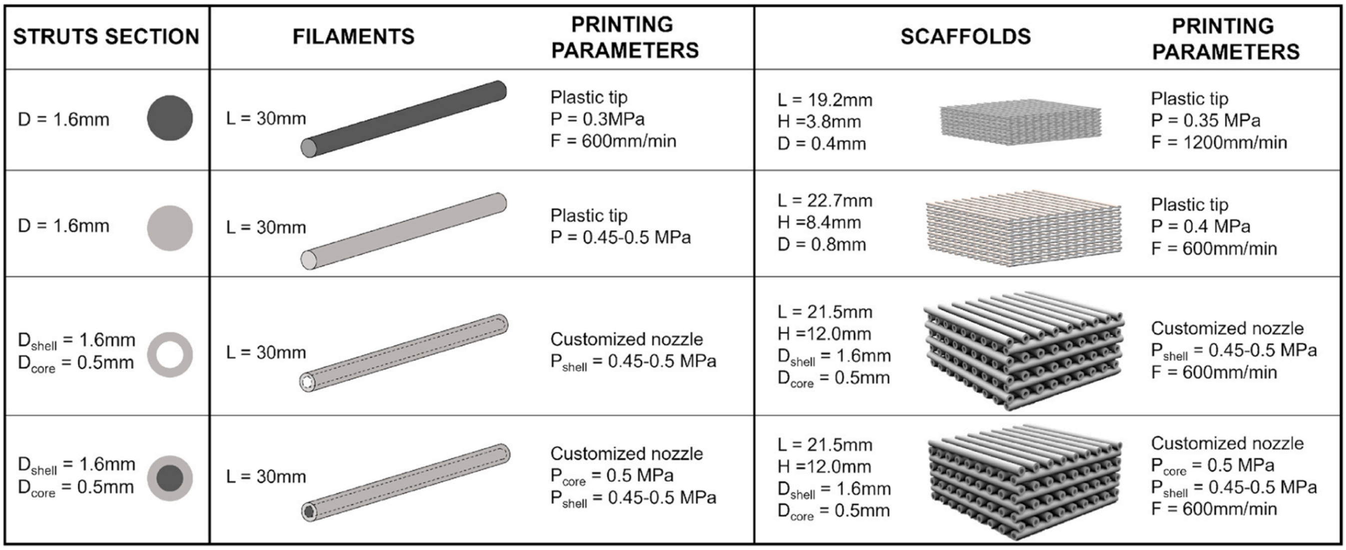

STRUTS SECTION	FILAMENTS	PRINTING PARAMETERS	SCAFFOLDS	PRINTING PARAMETERS
D = 1.6mm	L = 30mm	Plastic tip P = 0.3MPa F = 600mm/min	L = 19.2mm H =3.8mm D = 0.4mm	Plastic tip P = 0.35 MPa F = 1200mm/min
D = 1.6mm	L = 30mm	Plastic tip P = 0.45-0.5 MPa	L = 22.7mm H =8.4mm D = 0.8mm	Plastic tip P = 0.4 MPa F = 600mm/min
D_{shell} = 1.6mm D_{core} = 0.5mm	L = 30mm	Customized nozzle P_{shell} = 0.45-0.5 MPa	L = 21.5mm H =12.0mm D_{shell} = 1.6mm D_{core} = 0.5mm	Customized nozzle P_{shell} = 0.45-0.5 MPa F = 600mm/min
D_{shell} = 1.6mm D_{core} = 0.5mm	L = 30mm	Customized nozzle P_{core} = 0.5 MPa P_{shell} = 0.45-0.5 MPa	L = 21.5mm H =12.0mm D_{shell} = 1.6mm D_{core} = 0.5mm	Customized nozzle P_{core} = 0.5 MPa P_{shell} = 0.45-0.5 MPa F = 600mm/min

Fig. 1. Illustration of the fabricated geometries and printing parameters. The reference study previously conducted on 316L solid scaffolds is reported in [36].

and the presence of secondary phases such as perovskite [32]. Applying the same conditions also allowed the investigation of the influence of different $CaTiSiO_5$ precursors on the final properties.

2.5. Microstructural and mechanical characterization

The fabricated samples were weighed and measured with a digital caliper both before and after the heat treatment, to assess mass loss and dimensional shrinkage. Once sintered, a porosity analysis of the samples was conducted. The samples were impregnated with distilled water for 18 min [37], and the apparent porosity was measured using the Archimedes' method. Closed porosity was then determined by comparing bulk density (mass over total volume of samples), apparent density, and theoretical density. The theoretical density of both 316L and $CaTiSiO_5$ solid samples was measured by a He-pycnometer (UltraPyc 3000, Anton Paar, Graz, Austria), and values were 7.94 g/cm^3 and 3.49 g/cm^3 , respectively. In the case of core–shell samples, the theoretical density was calculated according to the rule of mixtures, based on the relative amounts of steel and sphene measured from cross-section images captured using a stereo optical microscope (AxioCamERc 5 s Microscope Camera, Carl Zeiss Microscopy, US) and processed using ImageJ software. The total porosity was finally calculated as the sum of the apparent and the closed porosities.

To confirm the correct synthesis of sphene from the selected precursors, X-ray Diffraction analyses (XRD) were conducted on the crushed powders of sintered sphene components (Bruker D8 Advance diffractometer, Bruker, Karlsruhe, Germany) with Cu-Kα radiation ($\lambda = 1.541874$ Å), over a 2θ range of 10°–70°, with a step size of 0.05°. Phase identification was conducted using the Match! program package (Crystal Impact GbR, Bonn, Germany) and was supported by data from PDF−2 database (ICDD-International Centre for Diffraction Data, Newtown Square, PA, USA). The morphology of the samples was investigated, as well as the quality of the metal–ceramic interface; to this end, sintered filaments and scaffolds were embedded in resin, and their cross-sections were subsequently polished and analyzed by scanning electron microscopy (SEM) (Quanta FEI, Eindhoven, The Netherlands) coupled with energy-dispersive X-ray spectroscopy (EDS) (Thermo Scientific, UltraDry).

Further analyses were performed to assess the mechanical behavior of the sintered components. The sintered filaments were subjected to four-point bending tests performed at a crosshead speed of 0.5 mm/min (Quasar 25, 25000 N maximum load, Galdabini S.p.a., Cardano al Campo, Italy). The flexural strength was determined using the following equation:

$$\sigma_{nominal} = \frac{4FLD}{\pi\left(D^4 - D_{core}^4\right)} \quad (1)$$

where F is the applied load, L is the length between the two lower contact points, D is the outer diameter of the filament and D_{core} is the diameter of the inner metallic core. The compressive strength, calculated as the ratio between the applied load and the cross-sectional area, was evaluated through compression tests performed on the scaffolds at a crosshead speed of 0.5 mm/min. At least 5 specimens were fabricated and tested for each test condition and sample type. To prevent slipping phenomena between the specimens and the compression plates, a thin layer of parafilm was placed on the top and bottom surfaces of the samples. From the recorded load-displacement curves, engineering stress-strain curves were derived, from which the compressive strength (for brittle samples) or the yield stress (for ductile samples), the elastic modulus (determined as the slope of the linear elastic region of the stress-strain curve [38]), and strain energy density (calculated as the area under the stress-strain curve [38]) were derived.

2.6. Evaluation of the in vitro bioactivity in SBF

The bioactivity of the samples was tested in vitro in SBF, an acellular solution mimicking human plasma. SBF was prepared following the protocol by Kokubo et al. [39]. The pH was adjusted to 7.4 using HCl or NaOH. Scaffolds (5 mm x 5 mm x 5 mm in the case of mono-material lattices, 8 mm x 8 mm x 10 mm in the case of composite lattices) were immersed in SBF at a weight-to-volume ratio of 10 mg/mL and incubated at 37 °C. The solution was periodically refreshed, as recommended in the literature, to roughly simulate physiological fluid turnover, and its pH was measured at each change. Samples were collected after 1, 3, and 7 days, rinsed with bidistilled water, and dried at room temperature. Sample morphology was examined using two SEMs (FEI Co., Eindhoven, The Netherlands): a Quanta 2000 environmental SEM (ESEM) and a Nova NanoSEM 450 field-emission gun SEM (FEG-SEM), the latter providing higher resolution for detailed surface observations. Surface composition was further analyzed by EDS (Inca, Oxford Instruments, Abingdon, UK). The possible formation of hydroxyapatite on the sample surfaces was analyzed by micro-Raman spectroscopy using a LabRAM system (Horiba Jobin-Yvon, Villeneuve d'Ascq, France). The measurements were carried out with a 532 nm diode laser, while the Raman signal was dispersed through an 1800 lines/mm grating monochromator and detected by a CCD sensor. Spectra were collected using a 50 × Ultra Long Working Distance (ULWD) objective, with an acquisition protocol consisting of five accumulations of 30 s each.

2.7. *Measurement of ion release*

Ionic release from the scaffolds was evaluated in vitro by dissolution in SBF. For each test, the samples were immersed in SBF at a solid-to-liquid ratio of 10 mg/mL and incubated at 37 °C under static conditions. After 1, 3, and 7 days of immersion, the suspensions were filtered through 0.45 μm-pore membranes to remove residual nanoparticles. The filtrates were analyzed using triple-quadrupole inductively coupled plasma mass spectrometry (iCAP TQ ICP-MS; Thermo Fisher Scientific, Bremen, Germany). Scandium was used as an internal standard to minimize non-spectral interferences and ensure accurate quantification. Calibration curves were prepared using certified ionic standards, and diluted solutions were analyzed in triplicate. Ion concentrations are reported as mean ± standard deviation values.

2.8. *Cytotoxicity tests*

For the preparation of eluates, the produced scaffolds were incubated in Dulbecco Modified Eagle Medium (DMEM) (Thermo Fisher Scientific, MA, USA) at 37 °C for 16 h, according to the ISO 10993–12 guidelines [40]. Eluates were sterilized using 0.22 μm filters. The Balb/3T3 embryonic mouse fibroblast cell line (American Type Culture Collection, ATCC) was used as a standard model for cytotoxicity testing. Cells were seeded at a density of 10^4 cells/well in 96-well plates (Falcon, NY, USA) and cultured in DMEM supplemented with 10% fetal bovine serum, 1% penicillin-streptomycin and 1% non-essential amino acids (Thermo Fisher Scientific). After 24 h, the culture medium was replaced with eluates at different concentrations (i.e., 100%, 50%, 25% and 12.5%). Cells cultured in culture medium with or without 0.1% sodium dodecyl sulphate (SDS, Merck-Life Science) served as the positive and negative controls, respectively. After 24 h, cytotoxicity was assessed with the MTT assay as recommended in [41], as already described [42]. Two independent experiments were performed, each with six technical replicates, and the values are reported as mean ± standard deviation.

3. Results and discussion

3.1. *Rheological characterization and 3D-printing phase*

The results of the rheological analyses conducted on 316 L and $CaTiSiO_5$ inks are reported in Fig. 2 and Table 4.

The rheological properties of the two formulated inks were tuned to meet the printability requirements of core-shell structures. The 316L-based ink exhibits its LVR region up to 2 Pa, after which the yielding of the structure starts. This very low yield stress allows good control over the extrusion of the steel core, thereby maximizing its content in the composite printed structures by applying a high printing pressure (0.5 MPa). On the other hand, the $CaTiSiO_5$-based ink shows higher rheological characteristics, exhibiting an LVR region up to around 1000 Pa. This behaviour can be attributed to the use of glycerol in the formulation, whose action as a plasticizer is well known and provides the ink with a high degree of plasticity, while also enhancing the surface quality of the extruded struts, making them smoother [43,44]. Thanks to its high yield stress, this ink is ideal for extrusion through the shell channel, as it ensures good shape fidelity and structural support, preventing collapse even in multi-layer structures. The inks' recovery times also confirm their suitability for the extrusion channel. The 316L-based ink exhibits a recovery time exceeding 160 s, indicating that the reconstruction of its internal structure after extrusion is slow. However, this phenomenon does not represent an issue thanks to the faster recovery of the shell ink, which shows a recovery time of approximately 100 s and, therefore, allows the metallic core to be contained while maintaining the target shape.

Additional information regarding the rheological characterization of the inks (flow curves) and the control of the co-extrusion process (including the dimensional control of the extruded composite struts and the area occupied by the metallic core) is provided in Section S1 of the Supplementary Information. Video S1 shows how the printing process takes place.

Supplementary material related to this article can be found online at doi:10.1016/j.jeurceramsoc.2026.118595.

Table 4
Rheological properties of optimized inks.

Ink	η_0 [Pa s]	σ_Y [Pa]	σ_F [Pa]	t_{REC} [s]
316L	3.1×10^4	2.9	4.9	164
$CaTiSiO_5$	1.9×10^5	600	1294	101

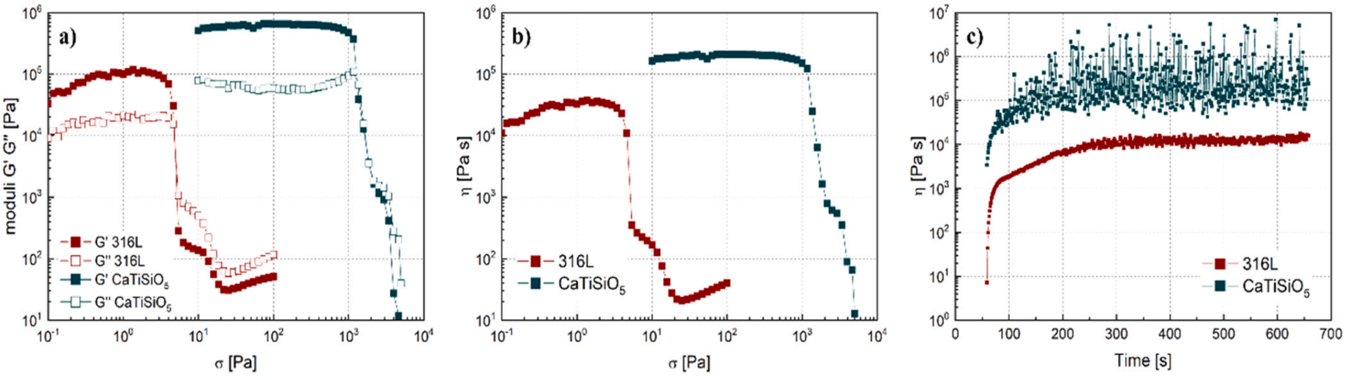

Fig. 2. Results of rheological analyses performed on 316L and $CaTiSiO_5$ inks.

3.2. Thermal debinding and sintering

The results of TGA-DTA analyses are reported in Fig. 3.

The mass loss of the 316L ink is 4% (Fig. 3a), corresponding to the polymer content of the ink. However, after 600 °C an abnormal weight increase is observed, due to oxygen infiltration into the instrument and the resulting oxidation of the metal. For the $CaTiSiO_5$ precursors ink, the mass loss is 16% (Fig. 3a) higher than the organic content of the mixture (around 13.4%). As reported in Fig. 4, the $CaSiO_3$ powders used in this work also contain secondary phases, such as $CaCO_3$ (that decomposes to CaO and CO_2 at $T > 600°C$) and SiO_2 that reacts with CaO to give $CaSiO_3$ at 800°C−900°C. The higher weight loss can then be attributed to the CO_2 release (~2 wt%) as well as to residual non-evaporated water for $T < 100°C$.

From the derivative curves reported in Fig. 3b, two peaks can be identified for the 316L ink, one at 270 °C and one at 400 °C, which are related to the decomposition of PEG and PVA contained in the binder, as previously reported in [36]. For the $CaTiSiO_5$ ink, three main peaks can be identified. The first one, at 200 °C, is associated with the decomposition of glycerol [45], while the second at 290 °C and the third at 380 °C can be attributed to the decomposition of the binder (PEG and PVA). A small peak between 600 °C and 700°C and the broader peak extending between 700°C and 1000°C can be attributed to $CaCO_3$ decomposition, being the tested sample a bulk drop of ink. As expected, no weight loss is associated with the reaction between wollastonite and titania to produce sphene.

The mass loss, geometric shrinkage, and total porosity of the sintered filaments and scaffolds are reported in Table 5 and Table 6.

The mass loss of the 316L ink is 4%, consistent with the results of TGA. The $CaTiSiO_5$ components (both solid and shell filaments and scaffolds) exhibit a higher mass loss, ranging from 18% to 19%, compared to 16% from TGA, likely due to residual solvent trapped in dried components before sintering. For the composite filaments and scaffolds, the measured mass loss is intermediate between that of mono-material steel and sphene components. The steel and sphene contents, described by the parameter *Vr* (defined as the core-volume-to-total volume ratio), are estimated by analyzing cross-section images using the software ImageJ. Based on the estimated volume fractions of steel and sphene ($Vr = 24\%$ for filaments and $Vr = 16\%$ for scaffolds), the expected mass losses are 14.6% for filaments and 15.7% for scaffolds. The mismatch between these values and the experimental results is likely due to imprecisions in the *Vr* estimation method, which assumes cylindrical struts and constant core-to-shell volume ratios.

Solid 316L filaments exhibit an isotropic shrinkage in both longitudinal and radial directions, since they were printed and sintered as a grid. This shape affected their contraction, comparable to that observed in [36], where specimens made of connected struts exhibited isotropic shrinkages. In contrast, both solid and shell $CaTiSiO_5$-based filaments, as well as the 316L-$CaTiSiO_5$ composite filaments, display a more pronounced shrinkage along the radial direction with respect to the longitudinal one, since they are not constrained by the grid and can freely shrink. Scaffold shrinkage in the x-y plane is isotropic, while along the z direction a higher contraction is detected due to the weight. 316L solid filaments exhibit lower porosity compared to $CaTiSiO_5$ solid and shell filaments, whilst composite filaments are characterized by an intermediate porosity value. Similarly, solid and shell $CaTiSiO_5$ scaffolds possess higher porosity than composite lattices. This trend is consistent with the 316L-$CaTiSiO_5$ architecture: the coexistence of a dense metallic core (~24 vol%) and a porous ceramic shell (~76 vol%) results in a total porosity that lies between that of the single materials.

3.3. Microstructural and morphological characterization

The results of XRD analyses performed on the sphene precursors and on the crushed sintered powders are reported in Fig. 4. The as-received wollastonite has minor amounts of $CaCO_3$ and SiO_2 likely due to the natural carbonatation reaction of the silicate. The TiO_2 nanopowders confirm anatase as the only phase. After sintering, the main peaks of the as-received wollastonite disappear, while significant variations in relative peak intensities are observed, indicating the occurrence of the expected phase transformation during thermal treatment. Wollastonite ($CaSiO_3$) is a single-chain silicate composed of SiO_4 tetrahedra, in which calcium occupies interstitial octahedral sites and is coordinated by six oxygen atoms [46]. The reaction between wollastonite and titania proceeds in the solid state starting at approximately 1100 °C [47]. In fact, the spectrum, corresponding to the sintered powders at 1240 °C in Fig. 4, clearly shows sphene ($CaTiSiO_5$) as the main phase. Perovskite $CaTiO_3$ is also detected as a secondary phase, consistent with what has been reported in [16], together with pseudowollastonite $Ca_3(Si_3O_9)$. Above 1125 °C, wollastonite undergoes a phase transition to pseudowollastonite, which exhibits a layered structure composed of alternating sheets of Si_3O_9 tri-tetrahedral rings and layers of distorted Ca-octahedra [48]. This suggests that, as the phase transition progressed, part of the wollastonite bypassed reaction with titania and subsequently stabilized as pseudowollastonite. The detection of rutile TiO_2 is also consistent with the presence of unreacted titania remaining in the system.

Fig. 5 shows the polished cross-sections of sintered filaments and scaffolds. The polished cross-section of the steel filament (Fig. 5a) shows a very compact matrix with the presence of residual porosity, likely related to the degradation of the organic content. The cross-sections of the solid and shell $CaTiSiO_5$ filaments (Figs. 5b and 5c respectively) exhibit a highly porous morphology, where two distinct pore

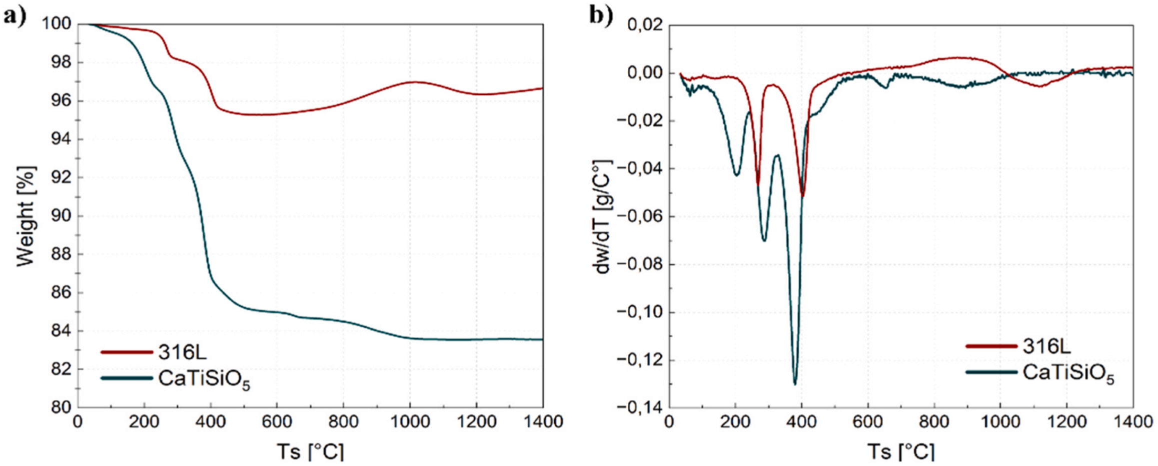

Fig. 3. Results of TGA-DTA analyses conducted on the dried inks.

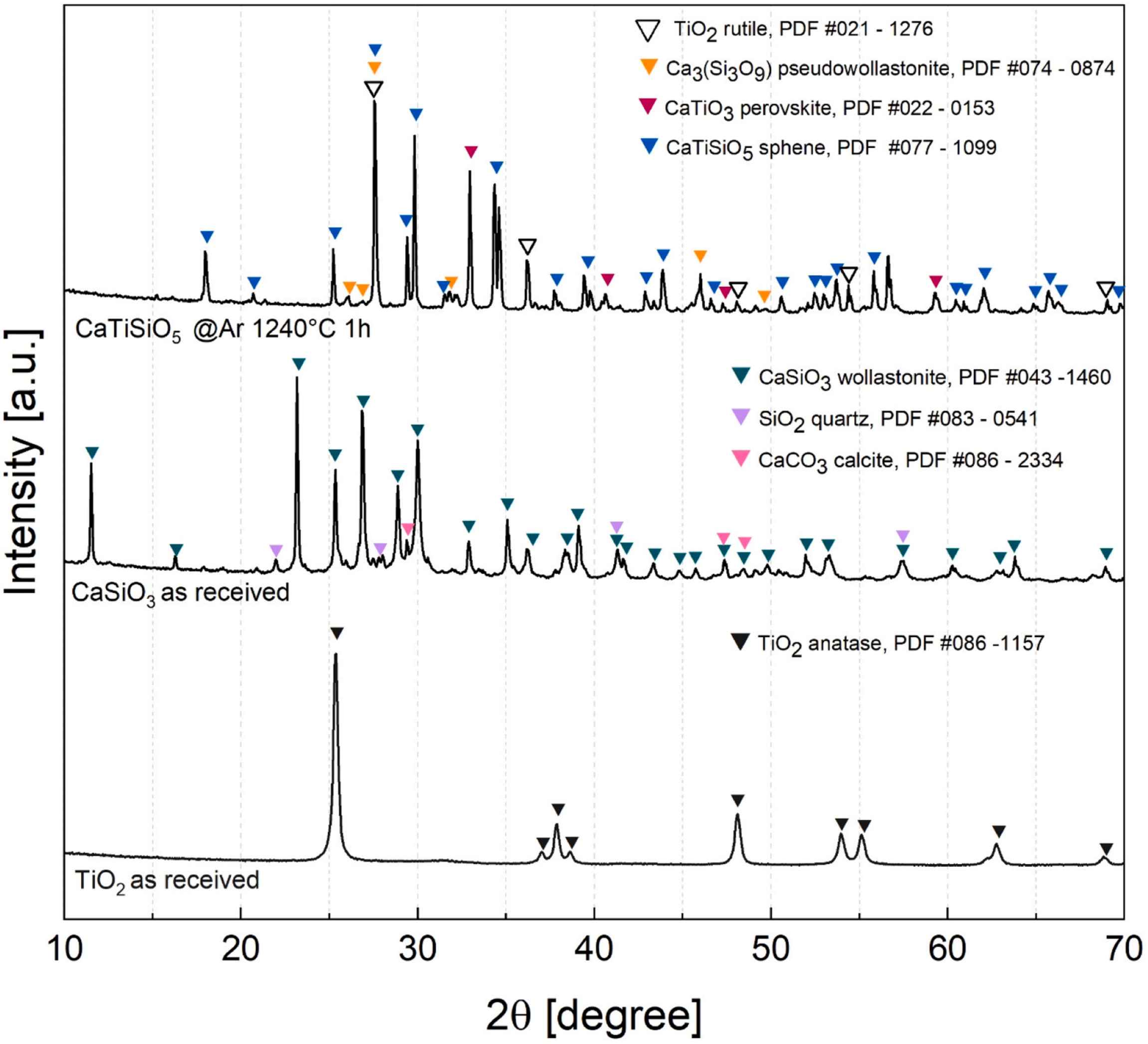

Fig. 4. XRD spectra of the starting precursors powders for sphene synthesis, and of the final crushed powders of sintered sphene components.

Table 5
Mass loss, geometric shrinkage and total porosity of sintered filaments.

Filament	Δm [%]	ΔL [%]	ΔD [%]	ΔV [%]	P_{tot} [%]
Solid 316L	4.0 ± 0.6	13.7 ± 0.9	14.2 ± 1.3	36.1 ± 1.9	12.1 ± 1.5
Solid $CaTiSiO_5$	18.5 ± 0.5	8.8 ± 0.8	20.9 ± 1.1	43.0 ± 1.8	40.1 ± 1.7
Shell $CaTiSiO_5$	18.3 ± 0.8	8.7 ± 1.5	20.0 ± 2.2	40.4 ± 5.7	51.5 ± 1.7
316L-$CaTiSiO_5$	11.9 ± 0.4	4.9 ± 0.9	19.8 ± 2.0	38.8 ± 3.0	37.4 ± 2.0

Table 6
Mass loss, geometric shrinkage and total porosity of sintered scaffolds.

Scaffold	Δm [%]	$ΔL_1$ [%]	$ΔL_2$ [%]	$ΔL_3$ [%]	ΔV [%]	P_{tot} [%]
Solid $CaTiSiO_5$	18.8 ± 0.3	9.5 ± 1.8	9.4 ± 1.1	15.5 ± 1.0	30.7 ± 2.0	76.4 ± 2.6
Shell $CaTiSiO_5$	19.3 ± 0.1	6.5 ± 1.9	5.5 ± 2.1	14.5 ± 2.5	16.9 ± 0.8	81.0 ± 2.2
316L-$CaTiSiO_5$	12.7 ± 0.6	5.0 ± 1.2	4.6 ± 0.9	13.6 ± 2.2	21.8 ± 2.4	73.2 ± 1.1

populations are identified through image analysis. The first consists of small, nearly circular pores with diameters generally below 10 μm, homogeneously distributed across the sample surface. The second population is characterized by larger pores with a more irregular morphology, exhibiting average dimensions of approximately 80 μm and occasionally reaching up to 150 μm. Unlike the smaller pores, these larger voids are distributed more randomly, resulting in localized regions enriched in large pores alternating with areas mainly characterized by smaller pores. This double pore size distribution may be attributed to binder decomposition and a partial inhomogeneity of the ink, even if further studies are necessary to better understand the solid load and binder distribution inside the ink.

The cross-section of the composite filament (Fig. 5d) highlights the irregular edges of the metal core, probably due to the interaction with the highly porous shell which induces localized concavities within the metallic matrix. Furthermore, the metallic core is slightly off-center with respect to the outer shell due to imperfect alignment of the nozzle channels, resulting in core misalignment. Figs. 5e and 5f, where solid and shell $CaTiSiO_5$ scaffolds are reported, confirm the suitability of ceramic ink's rheological properties, which allow the fabrication of multi-layer structures capable of shape retention, both in the case of solid struts and hollow struts. Fig. 5g shows the polished section of a 316L-$CaTiSiO_5$ scaffold, where a continuous inner metallic core can be observed, even if some residual porosity related to a not-optimized defoaming process can be detected.

EDS map analyses reveal slight differences in the steel depending on

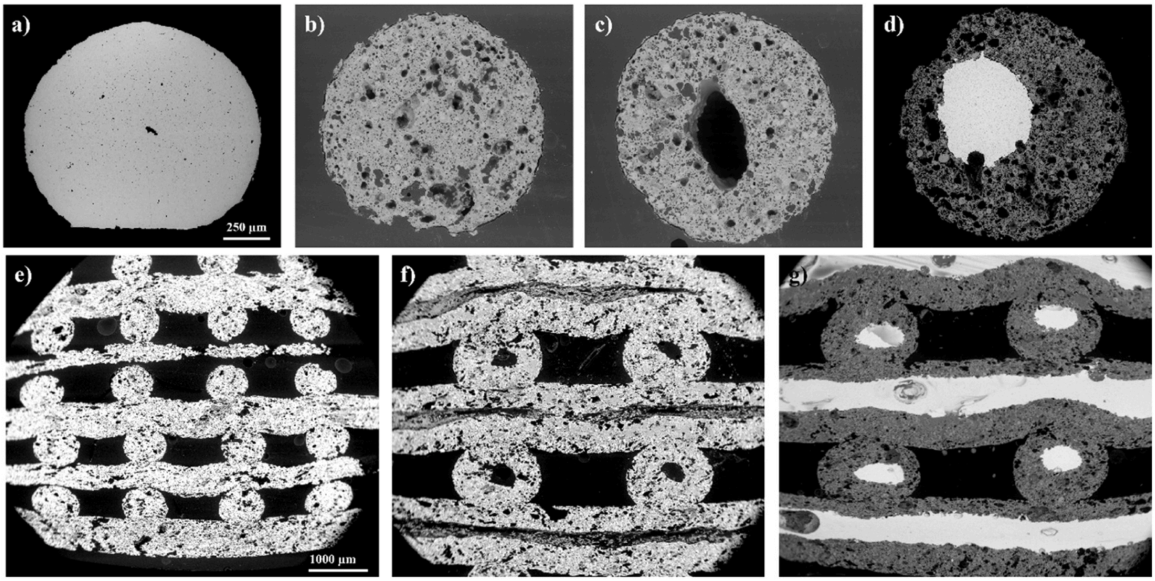

Fig. 5. SEM images of polished cross-sections of sintered samples: a–d) filaments (100 ×): solid 316L, solid $CaTiSiO_5$, shell $CaTiSiO_5$, and 316L–$CaTiSiO_5$ respectively; e–g) scaffolds (25 ×): solid $CaTiSiO_5$, shell $CaTiSiO_5$, and 316L–$CaTiSiO_5$ respectively.

whether it is sintered as a solid filament or together with the ceramic shell. In the former case (Figs. 6a and 6b), the matrix appears more compact, with some residual porosity and some areas exhibiting higher concentration of manganese and oxygen. When the steel is sintered together with the ceramic shell (Figs. 6c and 6d), both the closed porosity and the regions enriched in Mn and O are increased.

EDS analysis conducted on the cross-section of a solid $CaTiSiO_5$ filament highlights inhomogeneity related to the distribution of TiO_2, which tends to form distinct clusters clearly visible in the elemental map reported in Fig. 7. This tendency to aggregate can be attributed to van der Waals forces and capillary pressure acting during the dispersion of the powders in the aqueous-based polymeric binder. These forces are among the primary causes of heterogeneity, particularly when nano-sized powders are employed [49,50]. TiO_2-rich clusters, together with the high porosity of the structures, which may facilitate crack propagation, could act as local stress concentration sites and potentially influence the mechanical response of the material, particularly in regions where TiO_2 has not been fully incorporated into the sphene phase.

The synthesis reaction of sphene did not compromise the structure of the metallic matrix, unlike in a previous study using SiO_2, $CaCO_3$, and TiO_2 precursors [32], where CO_2 release during synthesis caused Cr and Mn migration to grain boundaries and the formation of non-passivating oxides, leading to steel embrittlement (Fig. 8a, red arrows). In the present work (Fig. 8b), the use of $CaSiO_3$ and TiO_2 precursors enabled sphene formation without CO_2 release, as wollastonite ($CaSiO_3$) replaced SiO_2 and $CaCO_3$, whose decomposition would otherwise generate CO_2. The EDS maps in Fig. 8a confirm the presence of Cr, Mn, and O at grain boundaries, highlighting the detrimental effect of CO_2 on sintering quality and the resulting brittleness of the composite struts. Conversely, in the present case, the sintering process yielded a compact steel matrix, where Cr and Mn, as well as all the other elements, are homogeneously distributed.

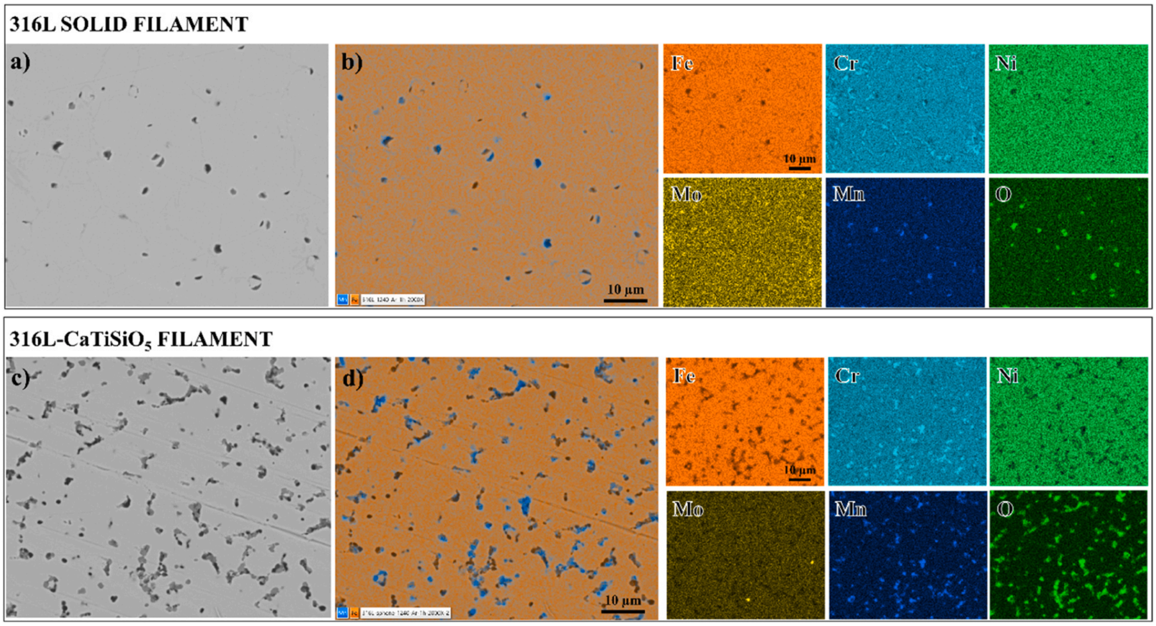

Fig. 6. SEM and EDS map analyses of: a) sintered solid 316L filament (2000x), b) sintered 316L filament with an outer $CaTiSiO_5$ shell (2000x).

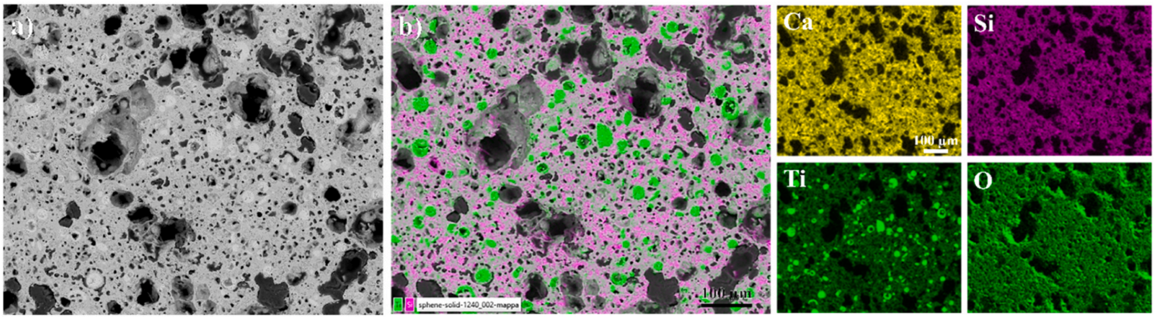

Fig. 7. SEM and EDS map analysis of the polished cross-section of a sintered $CaTiSiO_5$ solid filament (200x).

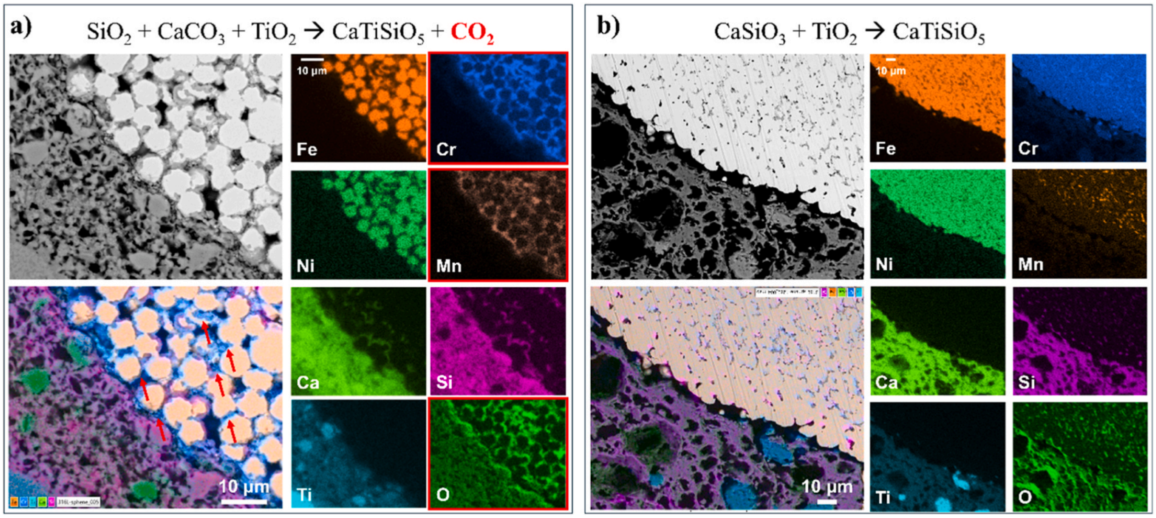

Fig. 8. SEM and EDS map analyses of 316L-$CaTiSiO_5$ metal-ceramic interface after sintering in the case of: a) previous work conducted using SiO_2, $CaCO_3$ and TiO_2 as precursors for sphene synthesis (5000x) – Reproduced from a previous publication by the authors [32], with permission. b) Actual work using $CaSiO_3$ and TiO_2 as precursors for sphene synthesis (1000x).

In Fig. 8a [32] perfect adhesion at the steel-ceramic interface was reached, whereas in Fig. 8b (present study), the bonding between 316L and $CaTiSiO_5$ is partial and characterized by a thin interfacial gap of irregular thickness measuring less than 10 µm. However, the rough morphology of the ceramic shell provides effective contact points with the metal core, thereby facilitating physical bonding between the phases. The lack of a more compact interface can be attributed to a lower shrinkage of the ceramic shell when $CaSiO_3$ and TiO_2 are used as precursors. The effect of the precursors on the volumetric shrinkage of the shell ink and on its compatibility with the steel ink was investigated through a systematic study of the inks' volumetric contraction. According to the literature [51], achieving good interfacial adhesion in sintered core–shell structures requires the presence of a compressive stress acting from the shell toward the core. To assess shrinkage compatibility between the inks, cubic specimens were fabricated by casting the inks into cubic molds, and their volumetric shrinkage after sintering was evaluated. The obtained results are reported below and compared with previously published data. In the previous study, the volumetric shrinkage of 316L ($\Delta V = 30.6 \pm 1.1\%$) was slightly lower than that of $CaTiSiO_5$ ($\Delta V = 33.7 \pm 1.8\%$), resulting in a compressive stress exerted by the shell on the core and leading to the formation of a well-adhered interface. In the present study, however, the shell ink exhibits a significantly lower volumetric shrinkage ($\Delta V = 26.2 \pm 1.9\%$) than the 316L core ink ($\Delta V = 33.8 \pm 0.7\%$). This reversed shrinkage relationship is likely responsible for the weaker adhesion observed at the metal–ceramic interface.

3.4. *Mechanical characterization*

The results of four-point bending tests conducted on filaments are reported in Fig. 9 and in Table 7.

The solid and shell $CaTiSiO_5$ filaments show a brittle behavior, with Young's modulus and maximum strength being slightly lower in the case of shell struts, because of the increased porosity related to the presence of the empty inner channel. The 316L solid filament shows its typical ductility, while the bending Young's modulus (~77 GPa) is lower than literature values (~130–140 GPa [52]), likely due to the presence of residual porosity; the maximum strength (797 MPa) is in accordance with literature data [52–54].

The composite 316L-$CaTiSiO_5$ filaments exhibit an intermediate behaviour between that of a ceramic and a metal. Their maximum flexural strength is about twice that of ceramic filaments, while the Young's modulus is comparable to that of shell struts (~30 GPa). The contribution of the metallic core becomes more evident when considering the deformability of the composite filaments: their strain energy density is two orders of magnitude higher than that of the ceramic struts. In the insets included in Fig. 9a, the brittle fracture mode of the pure ceramic phase can be observed, whereas the insets in Fig. 9b show how the 316L solid filament preserves its ductility, as does the 316L-$CaTiSiO_5$ composite, which, however, exhibits brittle fracture of the shell (the fracture modes are documented in video S2). These results provide a first indication that embrittlement of the 316L core can be prevented under the adopted processing conditions. Using $CaCO_3$ as CaO source for $CaTiSiO_5$, as reported in [32], the 316L-$CaTiSiO_5$ core-shell filament

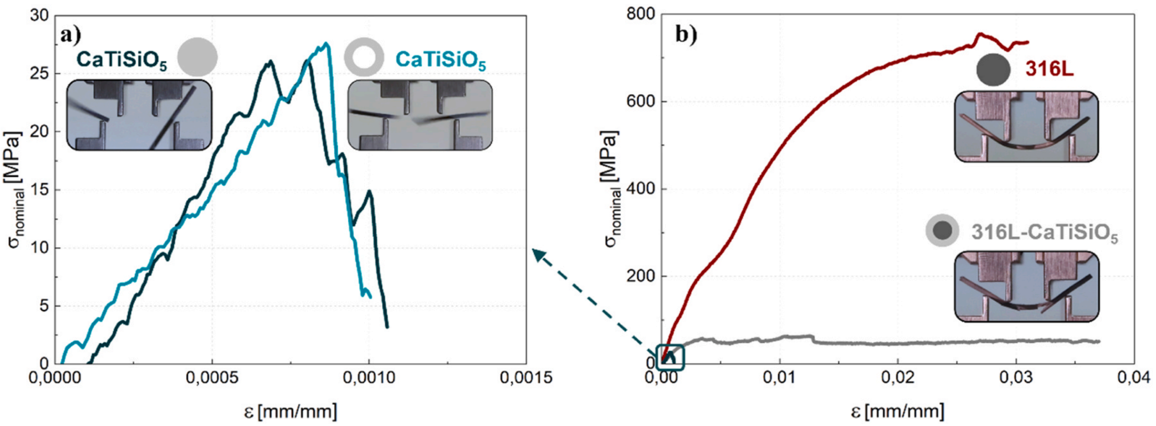

Fig. 9. Stress-strain curves of four-point bending tests performed on sintered filaments; a) $CaTiSiO_5$ full and shell filaments; b) 316L full and 316L-$CaTiSO_5$ core-shell filaments.

Table 7
Maximum nominal strength σ_{max} (corresponding to the maximum stress reached for metallic filaments, and to the failure stress for ceramic and composite filaments), bending modulus E (equal to the slope of the first linear part of the stress-strain curve) and strain energy density (area enclosed by the stress-strain curve) of sintered filaments.

Filament	σ_{max} [MPa]	E [GPa]	Strain Energy Density [MJ/m^3]
Solid 316L	797 ± 68	77 ± 14	18.000 ± 3.810
Solid $CaTiSiO_5$	36 ± 7	47 ± 6	0.014 ± 0.005
Shell $CaTiSiO_5$	32 ± 5	33 ± 7	0.014 ± 0.003
316L-$CaTiSiO_5$	76 ± 20	30 ± 5	2.260 ± 0.470

exhibited a brittle behaviour, with an average bending strength of 65.7 MPa with a broad deviation from the average.

Supplementary material related to this article can be found online at doi:10.1016/j.jeurceramsoc.2026.118595.

The curves and the results obtained from the compression tests performed on solid, shell $CaTiSiO_5$ and composite scaffolds are reported in Fig. 10a and Table 8.

The results obtained for mono-material ceramic lattices are comparable; the influence of the empty struts is negligible, as illustrated in Fig. 10a, where the dark blue and light blue curves are almost overlapping. The composite scaffolds exhibited higher Young's modulus and compressive strength, confirming the positive contribution of the inner metallic core, whose presence allows loads exceeding more than twice those achievable with scaffolds made of ceramic. Moreover, their compressive strength matches the values of cancellous bone (2–12 MPa) [1]. The strain energy density, which is similar for solid and shell $CaTiSiO_5$ scaffolds, is four times higher in the composite lattices, showing good agreement with the typical values of cancellous bone, usually ranging from 1 MJ/m^3 up to 7 MJ/m^3 [24]. Compared to our previous study [32] the strain energy density is 34.7% higher, thus confirming that the work performed by the core-shell composite during

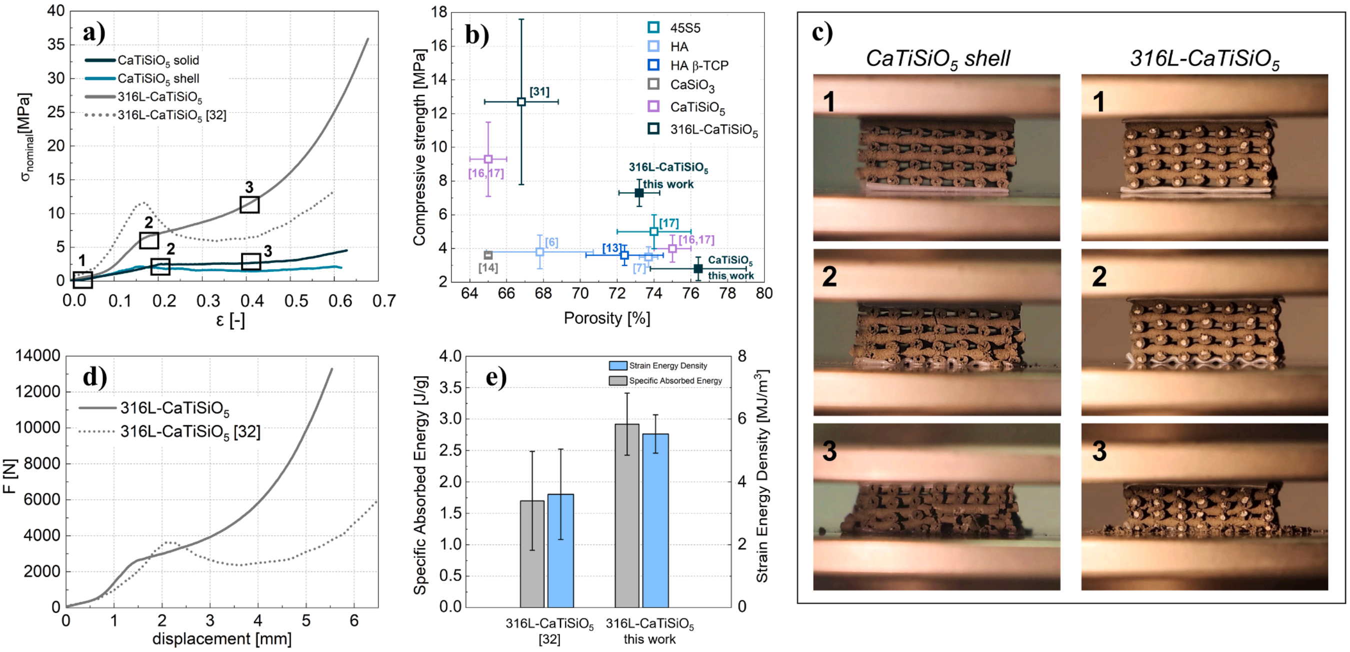

Fig. 10. a) average stress-strain compression curves of sintered scaffolds fabricated in this work and in the previous study [32]; b) comparison of scaffolds compressive strength produced using: hydroxyapatite [6,7], HA-β-TCP [13], $CaSiO_3$ [14], $CaTiSiO_5$ [15,16], Bioglass® 45S5 [17], 316L-$CaTiSiO_5$ [32], $CaTiSiO_5$ and 316L-$CaTiSiO_5$ of the current study; c) fracture events captured during the tests and corresponding points on stress-strain curves; d) average force-displacement compression curves of 316L-$CaTiSiO_5$ scaffolds fabricated in the present study and in the previous study [32], and e) corresponding specific adsorbed energy and strain energy density.

Table 8

Maximum nominal strength σ_{max} (corresponding to the maximum stress reached before the change in the slope of the curve), compression modulus *E*, strain energy density, and specific absorbed energy of sintered scaffolds.

Scaffold	σ_{max} [MPa]	E [MPa]	Strain Energy Density [MJ/m^3]	Specific Absorbed Energy [J/g]
Solid $CaTiSiO_5$	2.8 ± 0.7	13.1 ± 2.8	1.29 ± 0.36	1.00 ± 0.18
Shell $CaTiSiO_5$	2.3 ± 0.7	16.6 ± 3.8	0.89 ± 0.27	1.01 ± 0.23
316L-$CaTiSiO_5$	7.3 ± 0.8	60.8 ± 13.3	5.53 ± 0.61	2.92 ± 0.49
316L-$CaTiSiO_5$ [31]	12.7 ± 4.9	69.8 ± 20	3.61 ± 1.44	1.70 ± 0.79

compression occurs predominantly in the plastic region. The analysis of the failure mode of the shell $CaTiSiO_5$ and core-shell 316L-$CaTiSiO_5$ scaffolds (Fig. 10c) shows that in the case of shell $CaTiSiO_5$ scaffolds, vertical cracks occur within the struts, whereas for 316L-$CaTiSiO_5$ scaffolds, progressive densification is observed, with oblique cracks occurring in the shell (Video S3).

Supplementary material related to this article can be found online at doi:10.1016/j.jeurceramsoc.2026.118595.

Fig. 10b presents a comparison between the compressive strength values reported in the literature and those obtained in the present study. Solid $CaTiSiO_5$ scaffolds exhibit slightly lower, yet comparable, compressive strength and higher porosity compared to other bioceramic and bioactive glass scaffolds. In contrast, 316L–$CaTiSiO_5$ scaffolds, when compared with bioceramic scaffolds of similar porosity, display significantly higher compressive strength, which can be attributed to the presence of the metallic core. Compared to our previous study [32], the samples investigated here exhibit a higher porosity (73% vs. 67%), resulting in a lower compressive strength and a lower variance, thereby confirming the improved consistency and quality of the proposed synthesis process.

The composite scaffolds produced in the present study exhibit higher specific absorbed energy [55] and strain energy density values compared to those fabricated previously, where the contribution of the metallic core was impaired by oxidation (Fig. 10d and 10e).

The role of residual stresses generated during the synthesis and sintering process upon cooling is a key aspect in composite materials, especially in the presence of a mismatch in the coefficient of thermal expansion between the two materials used as the matrix and reinforcement (shell and core in this study, respectively). In addition, when extrusion-based AM technologies are used, linear and volumetric shrinkage are key issues, as shown in [28] where linear shrinkage was affected by the 3D printing strategy. Studies are ongoing to better clarify this issue.

3.5. *Assessment of in vitro bioactivity and cytotoxicity test*

The bioactivity of the produced scaffolds was tested *in vitro* by immersing them in SBF for periods ranging from 1 to 7 days. In parallel, the pH of the solution was monitored as an indicator of the intensity of ionic-exchange processes between the samples and the medium, and the release of selected ions was quantified by ICP-MS TQ. The SBF solution was prepared according to the original Kokubo protocol, later

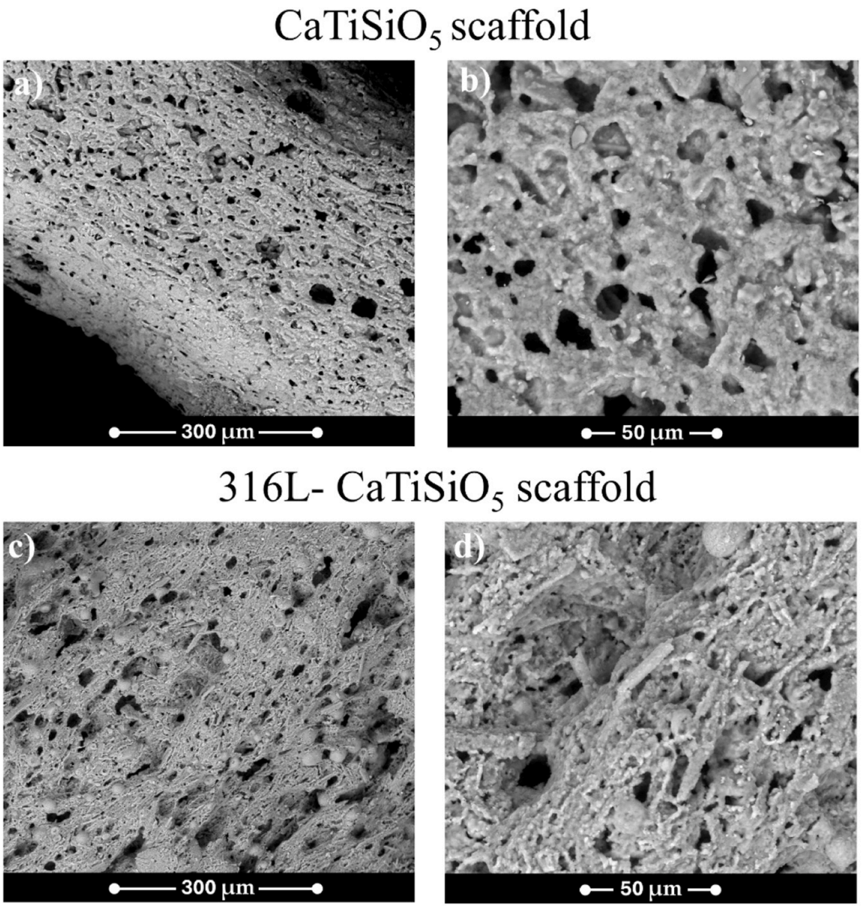

Fig. 11. SEM images of the surface of samples $CaTiSiO_5$ (a, b) and 316L-$CaTiSiO_5$ (d–f) before immersion in SBF. Images (a) and (c) were acquired at a magnification of 400 × , whereas images (b) and (d) were acquired at 1600 × .

formalized in the ISO 23317:2025 standard for the initial screening of apatite-forming ability of bone-contacting implant materials [56]. Although the ISO standard provides a more formalized procedure, the Kokubo method is still widely adopted for preliminary bioactivity screening, and the experimental conditions used in this study are consistent with those prescribed by the standard.

For comparison purposes, SEM micrographs of the as-prepared samples prior to SBF immersion are reported in Fig. 11, in order to highlight the surface morphology of the control specimens before the bioactivity tests. SEM observations of the $CaTiSiO_5$ scaffolds (Fig. 11a, b) revealed a highly porous and heterogeneous surface morphology, characterized by the presence of interconnected macro- and micropores distributed throughout the structure. Such porosity is considered particularly favorable for biomedical applications, as it may promote fluid penetration, ion exchange, and subsequent cell colonization. A comparable morphology was also observed in the 316L-$CaTiSiO_5$ samples (Fig. 11c, d), indicating that the presence of the metallic core did not significantly alter the surface architecture of the ceramic component. At higher magnification, both systems exhibited a rough and irregular surface texture, which is expected to increase the specific surface area available for interaction with the physiological environment. Overall, the developed scaffolds displayed morphological features potentially suitable for bone tissue engineering applications, combining an interconnected porous structure with a surface topography favorable for biological interactions and ion-mediated bioactive processes.

Fig. 12 shows SEM images of the sample surfaces after 7 days of immersion in SBF. A clear difference in reactivity is observed between $CaTiSiO_5$ and 316L-$CaTiSiO_5$ scaffolds. While the former appears almost completely covered by globular precipitates with the typical cauliflower-like morphology of *in vitro*-formed HA, the 316L-$CaTiSiO_5$ scaffolds exhibit only sparse and fine precipitates, locally detectable and mainly visible at higher magnification. In the $CaTiSiO_5$ samples, the deposited layer appears relatively homogeneous over large surface areas, suggesting a more intense ionic exchange with the surrounding medium and a higher nucleation rate of calcium-phosphate phases. The EDS analysis reported in Fig. 12d confirms the calcium–phosphate nature of the precipitates, whose composition suggests a possible evolution toward HA. The EDS spectrum reported in Fig. 12d yielded a Ca/P atomic ratio of approximately 1.61, close to the stoichiometric value of HA (1.67). Nevertheless, this value should be considered only as a semi-quantitative indication, since the technique is inherently local and subject to variability related to the heterogeneous and globular morphology of the precipitated layer, as well as to possible contributions from the underlying substrate. Therefore, although the measured Ca/P ratio is compatible with the formation of HA-like calcium–phosphate phases, a precise stoichiometric assignment cannot be inferred from EDS analysis alone.

In contrast, the lower amount of precipitates observed on the 316L-$CaTiSiO_5$ scaffolds indicates a reduced surface reactivity under the adopted test conditions. The precipitation process appears more limited and less homogeneous than in the mono-material $CaTiSiO_5$ scaffolds, suggesting a delayed formation of calcium–phosphate phases on the composite structures. This different behavior is further supported by the EDS analyses performed on the surface of the 316L-CaTiSiO5 samples, which in several regions – as shown in the example reported in Fig. 12h – revealed only elements attributable to sphene, with no detectable calcium–phosphate phases. These findings suggest that, after 7 days of immersion, the precipitation process on the 316L-based scaffolds remains at an early stage and is not yet sufficiently developed to form a continuous mineralized layer.

SEM observations performed after shorter immersion times confirmed the slower evolution of the mineralization process. After 3 days of immersion, only limited calcium-phosphate precipitation was detected on $CaTiSiO_5$ scaffolds, while almost no surface deposits were observed on 316L-$CaTiSiO_5$ samples. The corresponding SEM and EDS analyses are provided in the Supplementary Material (Figures S5 and S6). At 1 day of immersion, no appreciable signs of surface mineralization were detected for either sample type.

Raman micro-spectroscopy provided evidence that, in selected regions of the $CaTiSiO_5$ samples, the calcium–phosphate precipitates locally evolved towards carbonated apatite after 7 days of immersion. In particular, Raman spectra acquired locally from globular precipitates on the sample surface displayed the characteristic features of carbonated apatite, as shown in Fig. 13. In fact, the spectrum exhibits the

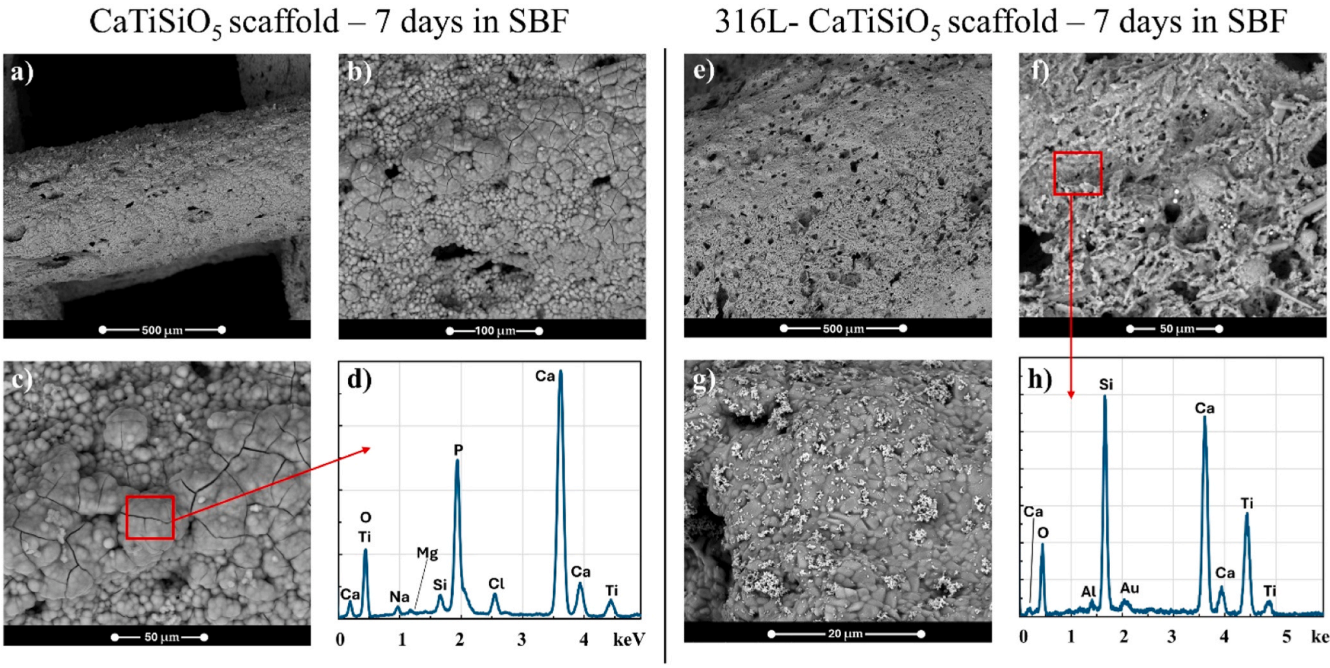

Fig. 12. SEM images of the surface of samples $CaTiSiO_5$ (a-c) and 316L-$CaTiSiO_5$ (e–g) after immersion in SBF for 7 days. The EDS spectra acquired from the areas indicated in (c) and (f) are shown in (d) and (h), respectively. Images (a) and (e) were acquired at 200 × , image (b) at 800 × , images (c) and (f) at 1600 × , and image (g) at 8000 × .

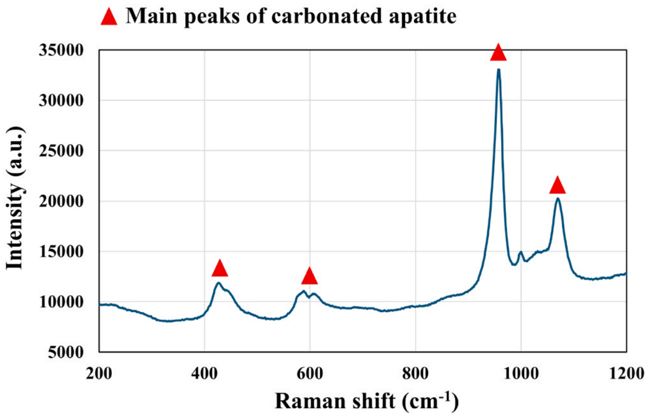

Fig. 13. Typical Raman spectrum acquired from globular precipitates formed on the surface of $CaTiSiO_5$ scaffolds after 7 days in SBF.

characteristic phosphate bands at approximately 430–450 cm^{-1}, 580–610 cm^{-1}, and the intense PO_4^{3-} band around 960 cm^{-1}, together with the carbonate-related band near 1070 cm^{-1}, typically associated with carbonated apatite [57–59]. This suggests that the surface of the $CaTiSiO_5$ scaffolds is not uniformly covered by apatite after 7 days, but rather by calcium–phosphate deposits that, in specific localized areas, may undergo further maturation towards a carbonated apatite-like phase.

The pH trend of the SBF (Fig. 14) also confirms the higher reactivity/bioactivity of $CaTiSiO_5$ scaffolds compared with the 316L-counterparts. As predicted by the widely accepted model described in the literature to explain the bioactivity of bioactive glasses and bioceramics [60], ionic-exchange processes involved in the surface dissolution of the materials in a physiological environment are expected to initially increase the pH of the solution. This phenomenon may raise biological concerns, since abrupt pH variations or excessively basic conditions can damage cells. Indeed, pH values exceeding 8.5 have been reported for certain materials, requiring *in vitro* preconditioning for several days before being brought into contact with cells [61]. From this standpoint, the scaffolds investigated in this study appear particularly promising, as the pH fluctuations never deviate significantly from the physiological range, even for the more reactive $CaTiSiO_5$ scaffolds.

Regarding ion release, we performed analyses for 8 ions (i.e., Si, Ca, P, Ti, Fe, Cr, Ni, and Mn). In line with the previous observations, the data show a higher release of silicon and calcium from the more reactive sphene scaffolds (Fig. 15a, b), whose surface tends to degrade more rapidly in SBF. For both $CaTiSiO_5$ and 316L-$CaTiSiO_5$ samples, the release of calcium and silicon reaches a maximum at 3 days and then decreases, consistent with the hypothesis of precipitation and/or reprecipitation from the solution in the form of calcium phosphates. Phosphorus was analyzed although it is not present in the scaffolds, but only in the SBF. As reported in the literature [62,63], a decrease in P concentration may indicate its interaction with calcium ions, leading to the formation of mineral deposits. In this study, a decrease of P was revealed, supporting the occurrence of calcium-phosphate complexes. Interestingly, the reduction in P was more marked for the $CaTiSiO_5$ compared to the 316L-$CaTiSiO_5$ sample. This difference may explain the SEM and EDS results, which showed a higher amount of mineral precipitates in the $CaTiSiO_5$ sample (Fig. 12). As for the release of the other investigated metal ions, ICP-MS analyses demonstrated low levels (e.g., values below 1 ppm for Fe, and in the ppb range for Cr, Mn, Ti, and Ni – see Fig. 13), remaining within ranges typically reported as non-cytotoxic in the literature. Indeed, cytotoxic effects of metallic ions such as Fe, Cr, and Mn are generally observed at significantly higher concentrations (typically in the μg/mL range or above), whereas trace concentrations in the ppb range are widely considered biocompatible and do not impair cell viability. For example, as verified by Hallab et al., 0.1 mM (≈10 ppm) was the highest non-toxic concentration for Cr, Ni, Co and 0.001 mM for Ti in lymphocyte assays, so the ppb level releases observed in this study are far below this limit. Hallab et al. also found serum Cr and Co concentrations of 0.3–0.7 μg mL^{-1} in hip arthroplasty patients were not associated with adverse cellular responses, further highlighting that the ppb levels we observe are non-toxic [64]. Geetha et al. described titanium alloys as highly biocompatible materials with lower cytotoxic potential than stainless steel and Co–Cr alloys. In light of the concentration-dependent and homeostasis-driven nature of metal ion toxicity, trace Ti release in the ppb range is unlikely to result in biologically relevant adverse effects [65]. Moreover, in their review, Lai et al. emphasized that the toxic effects of metal ions arise mainly from abnormal accumulation and loss of cellular homeostasis. Accordingly, the trace concentrations measured in the present study are unlikely to be biologically relevant in terms of toxicity [66].

On the other hand, since even minor changes in pH or ion concentration in the culture medium are well known to potentially induce cytotoxic effects, an MTT assay was performed using Balb/3T3 murine fibroblasts, in accordance with ISO 10993–5 and ISO 10993–12 guidelines [40,41].

The MTT assay is based on the ability of viable cells to reduce the yellow tetrazolium salt (MTT) to insoluble purple formazan crystals through mitochondrial enzymatic activity. The amount of formazan produced is directly proportional to the number of metabolically active cells and can therefore be quantified spectrophotometrically to assess cell viability after exposure to the sample extracts.

The results of the test are reported in Fig. 16. The MTT assay demonstrated the absence of cytotoxicity in Balb/3T3 cells cultured in the presence of different concentrations (i.e., 100%, 50%, 25%, and 12.5%) of eluates from both $CaTiSiO_5$ and 316L–$CaTiSiO_5$ scaffolds. As expected, the SDS-treated cells (positive control) displayed marked cytotoxicity.

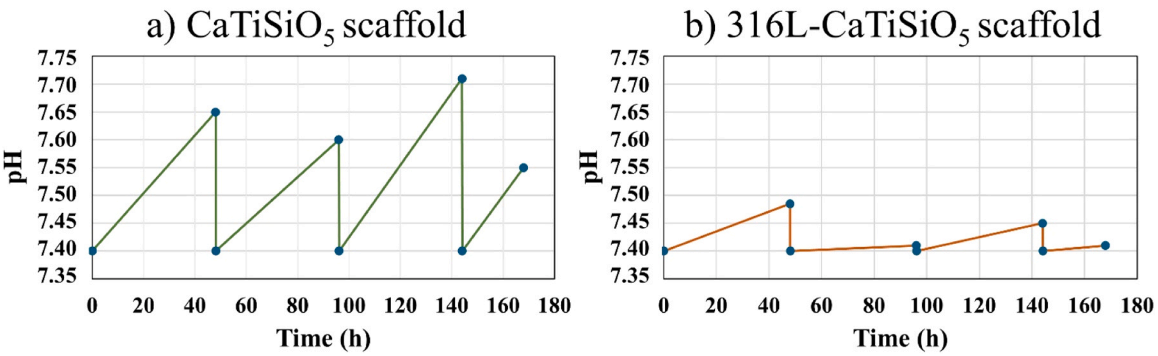

Fig. 14. pH variation induced by the produced scaffolds in SBF.

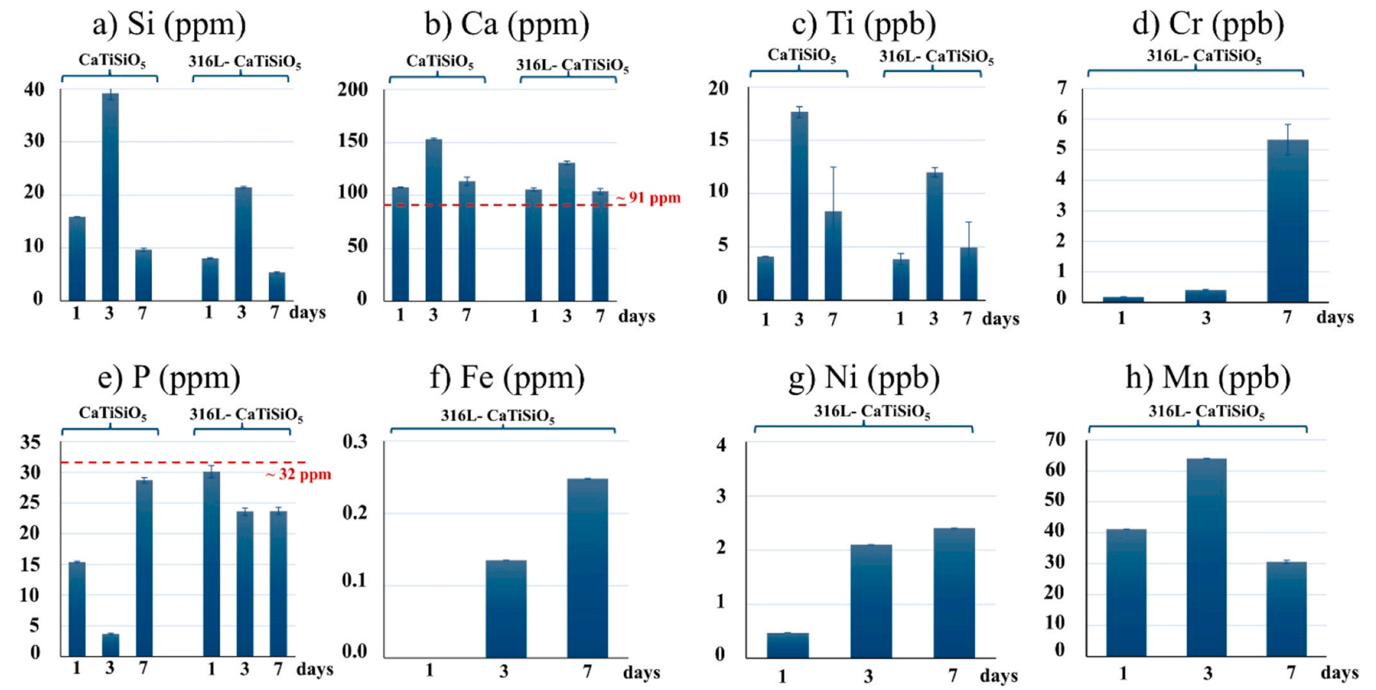

Fig. 15. Ion concentrations measured by ICP-MS TQ in SBF for $CaTiSiO_5$ and 316L-$CaTiSiO_5$ scaffolds. For calcium and phosphorus, the initial ion concentration in SBF is indicated by the red line; for the other ions, this initial concentration is assumed to be zero.

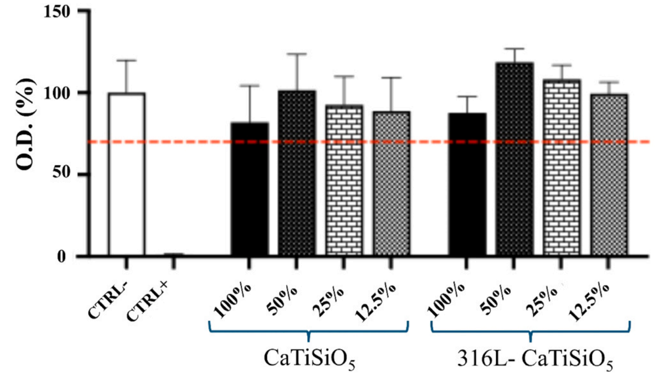

Fig. 16. The viability of the Balb 3T3 line was evaluated by the MTT test after 24 h of exposing in standard culture medium (DMEM, Ctrl-) or in the presence of different concentrations (100%, 50%, 25% and 12.5%) of eluates from the two different scaffolds. As a positive control (Ctrl +) cells were treated with DMEM + 0.1% SDS for 24 h. The optical density (O.D.) obtained in DMEM cultured cells was set as 100%. The red dotted line indicates the threshold value of 70%, compared to Ctrl-, that is required to demonstrate the absence of cytotoxicity, as defined by ISO 10993–5 protocol. Data are expressed as mean ± SD of two independent experiments performed in six replicates.

4. Conclusions

In this study, the fabrication of 316L-sphene ($CaTiSiO_5$) core-shell structures is reported. Inks were properly formulated to ensure continuous flows during co-extrusion. Mono-material and composite filaments and scaffolds were successfully sintered, showing good structural integrity and no cracks. Sphene was synthesized during sintering starting from $CaSiO_3$ and TiO_2 as precursors, using an almost CO_2-free process, thanks to which the steel microstructure was preserved from oxidation and showed its typical ductility. Sintered filaments and scaffolds were mechanically characterized: composite structures showed improved flexural and compressive performance compared to ceramic components, due to the positive contribution of the inner ductile core. In vitro tests confirmed the formation of calcium-phosphate phases, which may subsequently evolve into hydroxyapatite over time, in both $CaTiSiO_5$ and 316L–$CaTiSiO_5$ samples; however, a milder calcium phosphate formation was observed in the composite components. The absence of cytotoxicity was confirmed for all the tested samples. Overall, the composite samples exhibited superior mechanical properties compared to ceramic structures and comparable to cancellous bone, along with confirmed bioactivity and absence of cytotoxicity, demonstrating the potential of these structures to be applied as bone substitutes.

Declaration of Competing Interest

The authors declare that they have no known competing financial interests or personal relationships that could have appeared to influence the work reported in this paper.

Acknowledgments

This research was funded by MUR and EU– Next Generation EU with the project Multi-functional 3D printed bio-scaffolds, PRIN2022, MULTIFUN3D PROJECT, CUP C53D23001850006. Devis Bellucci and Valeria Cannillo wish to thank Dr. Simone De Micco and Dr. Andrea Martelli for their assistance during the in vitro tests in SBF, and Dr. Daniela Manzini for her help with the ionic release measurements performed using ICP-MS TQ.

Appendix A. Supporting information

Supplementary data associated with this article can be found in the online version at doi:10.1016/j.jeurceramsoc.2026.118595.

References

[1] S. Kanwar, S. Vijayavenkataraman, Design of 3D printed scaffolds for bone tissue engineering: a review, Bioprinting 24 (Dec. 2021) e00167, https://doi.org/10.1016/j.bprint.2021.e00167.

[2] A.J. Ashwin, J.M. Jafferson, State of the art direct ink writing (DIW) and experimental trial on DIW of HAp bio-ceramics, Mater. Today Proc. 46 (2021) 1298–1307, https://doi.org/10.1016/j.matpr.2021.02.396.

[3] Q. Zhou, X. Su, J. Wu, X. Zhang, R. Su, L. Ma, Q. Sun, R. He, Additive Manufacturing of Bioceramic Implants for Restoration Bone Engineering: Technologies, Advances, and Future Perspectives, ACS Biomater. Sci. Eng. 9 (3) (Mar. 2023) 1164–1189, https://doi.org/10.1021/acsbiomaterials.2c01164.

[4] C. Gautam, J. Joyner, A. Gautam, J. Rao, R. Vajtai, Zirconia based dental ceramics: structure, mechanical properties, biocompatibility and applications, Dalton Trans. 45 (48) (2016) 19194–19215, https://doi.org/10.1039/C6DT03484E.

[5] P. Srinath, P. Abdul Azeem, K. Venugopal Reddy, Review on calcium silicate-based bioceramics in bone tissue engineering, Int. J. Appl. Ceram. Technol. 17 (5) (Sep. 2020) 2450–2464, https://doi.org/10.1111/ijac.13577.

[6] M. Houmard, Q. Fu, M. Genet, E. Saiz, A.P. Tomsia, On the structural, mechanical, and biodegradation properties of HA/β-TCP robocast scaffolds, J. Biomed. Mater. Res. B Appl. Biomater. 101 (7) (Oct. 2013) 1233–1242, https://doi.org/10.1002/jbm.b.32935.

[7] Q. Liu, T. Li, S.W. Gan, S.Y. Chang, C.C. Yen, W. Zhai, Controlling the hierarchical microstructure of bioceramic scaffolds by 3D printing of emulsion inks, Addit. Manuf. 61 (Jan. 2023) 103332, https://doi.org/10.1016/j.addma.2022.103332.

[8] K. Liu, Q. Zhou, X. Zhang, L. Ma, B. Xu, R. He, Morphologies, mechanical and *in vitro* behaviors of DLP-based 3D printed HA scaffolds with different structural configurations, RSC Adv. 13 (30) (2023) 20830–20838, https://doi.org/10.1039/D3RA03080F.

[9] F. Baino, G. Magnaterra, E. Fiume, A. Schiavi, L.P. Tofan, M. Schwentenwein, E. Verné, Digital light processing stereolithography of hydroxyapatite scaffolds with bone-like architecture, permeability, and mechanical properties, J. Am. Ceram. Soc. 105 (3) (Mar. 2022) 1648–1657, https://doi.org/10.1111/jace.17843.

[10] D.L. Belgin Paul, A.S. Praveen, A. Arjunan, Parametric optimisation for 3D printing β-tricalcium phosphate tissue engineering scaffolds using direct ink writing, Smart Mater. Manuf. 3 (2025) 100070, https://doi.org/10.1016/j.smmf.2024.100070.

[11] D. Wang, J. Hou, C. Xia, C. Wei, Y. Zhu, W. Qian, S. Qi, Y. Wu, Y. Shi, K. Qin, L. Wu, F. Yin, Z. Chen, W. Li, Multi-element processed pyritum mixed to β-tricalcium phosphate to obtain a 3D-printed porous scaffold: An option for treatment of bone defects, Materials Science Engineering C 128 (Sep. 2021) 112326, https://doi.org/10.1016/j.msec.2021.112326.

[12] S. Liu, J. Chen, T. Chen, Y. Zeng, Fabrication of trabecular-like beta-tricalcium phosphate biomimetic scaffolds for bone tissue engineering, Ceram. Int. 47 (9) (May 2021) 13187–13198, https://doi.org/10.1016/j.ceramint.2021.01.184.

[13] J. Duan, H. Shao, H. Liu, J. Xu, M. Cong, K. Zhao, T. Lin, 3D gel-printing of hierarchically porous BCP scaffolds for bone tissue engineering, J. Eur. Ceram. Soc. 43 (6) (Jun. 2023) 2646–2653, https://doi.org/10.1016/j.jeurceramsoc.2023.01.010.

[14] C. Wu, W. Fan, Y. Zhou, Y. Luo, M. Gelinsky, J. Chang, Y. Xiao, 3D-printing of highly uniform CaSiO3 ceramic scaffolds: preparation, characterization and in vivo osteogenesis, J. Mater. Chem. 22 (24) (2012) 12288, https://doi.org/10.1039/c2jm30566f.

[15] H. Elsayed, L. Grigolato, G. Savio, P. Colombo, E. Bernardo, Direct ink writing of silicone/filler mixtures for sphene scaffolds with advanced topologies, Int. J. Appl. Ceram. Technol. 20 (1) (Jan. 2023) 131–140, https://doi.org/10.1111/ijac.14168.

[16] H. Elsayed, M. Sayed, S.M. Naga, P. Rebesan, C. Gardin, B. Zavan, P. Colombo, E. Bernardo, Additive manufacturing and direct synthesis of sphene ceramic scaffolds from a silicone resin and reactive fillers, J. Eur. Ceram. Soc. 42 (1) (Jan. 2022) 286–295, https://doi.org/10.1016/j.jeurceramsoc.2021.10.001.

[17] S. Eqtesadi, A. Motealleh, P. Miranda, A. Pajares, A. Lemos, J.M.F. Ferreira, Robocasting of 45S5 bioactive glass scaffolds for bone tissue engineering, J. Eur. Ceram. Soc. 34 (1) (Jan. 2014) 107–118, https://doi.org/10.1016/j.jeurceramsoc.2013.08.003.

[18] S.-B. Hua, J. Su, Z.L. Deng, J.M. Wu, L.J. Cheng, X. Yuan, F. Chen, H. Zhu, D.H. Qi, J. Xiao, Y.S. Shi, Microstructures and properties of 45S5 bioglass® & BCP bioceramic scaffolds fabricated by digital light processing, Addit. Manuf. Vol. 45 (Sep. 2021) . 102074, https://doi.org/10.1016/j.addma.2021.102074.

[19] W. Zou, X. Han, Q. Dai, Z. Lin, Q. Li, Z. Li, X. Xu, X. Chen, H. Gao, X. Cao, Three-dimensional-printed triply periodic minimal surface scaffolds via digital light processing for enhanced osteogenesis, Regen. Biomater. 12 (Jan. 2025), https://doi.org/10.1093/rb/rbaf053.

[20] L.L. Hench, Sol-gel materials for bioceramic applications, Curr. Opin. Solid. State Mater. Sci. 2 (5) (Oct. 1997) 604–610, https://doi.org/10.1016/S1359-0286(97)80053-8.

[21] N.E. Putra, M.J. Mirzaali, I. Apachitei, J. Zhou, A.A. Zadpoor, Multi-material additive manufacturing technologies for Ti-, Mg-, and Fe-based biomaterials for bone substitution, Acta Biomater. 109 (Jun. 2020) 1–20, https://doi.org/10.1016/j.actbio.2020.03.037.

[22] S. Li, Y. Huan, B. Zhu, H. Chen, M. Tang, Y. Yan, C. Wang, Z. Ouyang, X. Li, J. Xue, W. Wang, Research progress on the biological modifications of implant materials in 3D printed intervertebral fusion cages, J. Mater. Sci. Mater. Med. 33 (1) (Jan. 2022) 2, https://doi.org/10.1007/s10856-021-06609-4.

[23] I. Mitra, S. Bose, W.S. Dernell, N. Dasgupta, C. Eckstrand, J. Herrick, M. J. Yaszemski, S.B. Goodman, A. Bandyopadhyay, 3D Printing in alloy design to improve biocompatibility in metallic implants, Mater. Today 45 (May 2021) 20–34, https://doi.org/10.1016/j.mattod.2020.11.021.

[24] C. Paredes, F.J. Martínez-Vázquez, A. Pajares, P. Miranda, Novel strategy for toughening robocast bioceramic scaffolds using polymeric cores, Ceram. Int. 45 (15) (Oct. 2019) 19572–19576, https://doi.org/10.1016/j.ceramint.2019.06.175.

[25] A. Thomas, K.C.R. Kolan, M.C. Leu, G.E. Hilmas, Freeform extrusion fabrication of titanium fiber reinforced 13–93 bioactive glass scaffolds, J. Mech. Behav. Biomed. Mater. 70 (Jun. 2017) 43–52, https://doi.org/10.1016/j.jmbbm.2016.12.025.

[26] J. Ren, W. Xing, J. Wang, Q. Qian, H. Chen, D. Liu, N. Zhou, Multicore–Shell Direct Ink Writing of Coaxial Transmission Lines, ACS Appl. Eng. Mater. 2 (1) (Jan. 2024) 67–75, https://doi.org/10.1021/acsaenm.3c00573.

[27] M.A.S.R. Saadi, A. Maguire, N.T. Pottackal, M.S.H. Thakur, M.M. Ikram, A.J. Hart, P.M. Ajayan, M.M. Rahman, Direct Ink Writing: A 3D Printing Technology for Diverse Materials, Adv. Mater. 34 (28) (Jul. 2022), https://doi.org/10.1002/adma.202108855.

[28] L. Biasetto, V. Gastaldi, G. Bolzon, M. Farrokhtar, G. Franchin, Continuous fiber-like 316L-Al2O3 composites by one step co-extrusion 3D printing: an experimental and computational study, Ceram. Int. 52 (Mar. 2026) 6998–7010, https://doi.org/10.1016/j.ceramint.2025.12.447.

[29] M. Weichelt, L. Wahl, N. Travitzky, T. Fey, Co–extrusion of alumina core–shell structures fabricated by robocasting, Open. Ceram. 23 (Sep. 2025) 100805, https://doi.org/10.1016/j.oceram.2025.100805.

[30] Q. Cai, S. Meille, J. Chevalier, S. Zhou, F. Bouville, I. Tirichenko, E. Saiz, 3D-printing of ceramic filaments with ductile metallic cores, Mater. Des. 225 (Jan. 2023) 111463, https://doi.org/10.1016/j.matdes.2022.111463.

[31] Y. Luo, D. Zhai, Z. Huan, H. Zhu, L. Xia, J. Chang, C. Wu, Three-Dimensional Printing of Hollow-Struts-Packed Bioceramic Scaffolds for Bone Regeneration, ACS Appl. Mater. Interfaces 7 (43) (Nov. 2015) 24377–24383, https://doi.org/10.1021/acsami.5b08911.

[32] L. Biasetto, V. Gastaldi, H. Elsayed, Co-extrusion of highly loaded feedstocks for fabrication of stainless steel-bioceramic core-shell structures, J. Mater. Res. Technol. 33 (Nov. 2024) 6820–6830, https://doi.org/10.1016/j.jmrt.2024.10.255.

[33] H. Elsayed, G. Brunello, C. Gardin, L. Ferroni, D. Badocco, P. Pastore, S. Sivolella, B. Zavan, L. Biasetto, Bioactive Sphene-Based Ceramic Coatings on cpTi Substrates for Dental Implants: An In Vitro Study, Materials 11 (11) (Nov. 2018) 2234, https://doi.org/10.3390/ma11112234.

[34] G. Brunello, L. Biasetto, H. Elsayed, E. Sbettega, C. Gardin, A. Scanu, S. Carmignato, B. Zavan, S. Sivolella, An In Vivo Study in Rat Femurs of Bioactive Silicate Coatings on Titanium Dental Implants, J. Clin. Med. 9 (5) (Apr. 2020) 1290, https://doi.org/10.3390/jcm9051290.

[35] F. Baino, S. Yamaguchi, The Use of Simulated Body Fluid (SBF) for Assessing Materials Bioactivity in the Context of Tissue Engineering: Review and Challenges, Biomimetics 5 (4) (Oct. 2020) 57, https://doi.org/10.3390/biomimetics5040057.

[36] L. Biasetto, H. Elsayed, Direct Ink Writing of AISI 316L Dense Parts and Porous Lattices, Adv. Eng. Mater. 24 (11) (Nov. 2022), https://doi.org/10.1002/adem.202101729.

[37] Organization ISO, “Fine ceramics (advanced ceramics, advanced technical ceramics) — Determination of density and apparent porosity,” 2020.

[38] K.-C. Lai, K.K. Tseng, J.W. Yeh, S.H. Chen, Y.F. Song, G.C. Yin, P.Y. Chen, Super Energy Absorption of Lightweight Porous Al0.5CoCrFeNi2 High-Entropy Alloys Fabricated by Gas Atomization Plus Freeze-Casting Techniques, High. Entropy Alloy. & Mater. 3 (2) (Dec. 2025) 350–370, https://doi.org/10.1007/s44210-025-00070-6.

[39] T. Kokubo, H. Takadama, How useful is SBF in predicting in vivo bone bioactivity? Biomaterials 27 (15) (May 2006) 2907–2915, https://doi.org/10.1016/j.biomaterials.2006.01.017.

[40] Organization ISO, “Biological Evaluation of Medical Devices — Part 12: Sample Preparation and Reference Materials ISO 10993-12,” 2021.

[41] Organization ISO, “Biological Evaluation of Medical Devices - Part 5: Tests for In Vitro Cytotoxicity 10993-5 protocol.”

[42] D. Bellucci, A. Mazzilli, A. Martelli, F.G. Mecca, S. Bonacorsi, F.D. Lofaro, F. Boraldi, D. Quaglino, V. Cannillo, Enrichment of strontium and magnesium improves the physical, mechanical and biological properties of bioactive glasses undergoing thermal treatments: New cues for biomedical applications, Ceram. Int. 50 (24) (Dec. 2024) 52819–52837, https://doi.org/10.1016/j.ceramint.2024.10.135.

[43] S.S. Hossain, F. Akhtar, Development of tunable porous alumina monolith using hollow microspheres via extrusion-based 3D printing, J. Eur. Ceram. Soc. 44 (11) (Sep. 2024) 6620–6628, https://doi.org/10.1016/j.jeurceramsoc.2024.04.020.

[44] S.S. Hossain, F. Akhtar, Development of lightweight architecture of geopolymer via extrusion-based 3D printing for CO2 capture, J. Eur. Ceram. Soc. 45 (7) (Jul. 2025) 117191, https://doi.org/10.1016/j.jeurceramsoc.2025.117191.

[45] S.L. Barbosa, M.S. de Freitas, W.T.P. dos Santos, D.L. Nelson, M.B. de Freitas Marques, S.I. Klein, G.C. Clososki, F.J. Caires, E.J. Nassar, L.D. Zanatta, F. A. Agbleyor, C.A.M. Afonso, A.C. Moraes Baroni, Preparation of activated charcoal from Acrocomia aculeata for purification of pretreated crude glycerol, Biomass-.-. Convers. Biorefin 12 (7) (Jul. 2022) 2441–2449, https://doi.org/10.1007/s13399-020-00745-7.

[46] Y.V. Seryotkin, E.V. Sokol, S.N. Kokh, Natural pseudowollastonite: Crystal structure, associated minerals, and geological context, –135, Lithos 134 (Mar. 2012) 75–90, https://doi.org/10.1016/j.lithos.2011.12.010.

[47] D. Xirouchakis, S. Fritsch, R.L. Putnam, A. Navrotsky, D.H. Lindsley, Thermochemistry and the enthalpy of formation of synthetic end-member (CaTiSiO5) titanite, Am. Mineral. 82 (1997) 754–759, https://doi.org/10.2138/am-1997-7-813.

[48] H. Yang, C.T. Prewitt, On the crystal structure of pseudowollastonite (CaSiO3), Am. Mineral. 84 (1999) 929–932.

[49] H.S. Bae, M.K. Lee, W.W. Kim, C.K. Rhee, Dispersion properties of TiO2 nano-powder synthesized by homogeneous precipitation process at low temperatures, Colloids Surf. A Physicochem. Eng. Asp. 220 (1–3) (Jun. 2003) 169–177, https://doi.org/10.1016/S0927-7757(03)00077-3.

[50] J.-P. Boisvert, J. Persello, J.-C. Castaing, B. Cabane, Dispersion of alumina-coated TiO2 particles by adsorption of sodium polyacrylate, Colloids Surf. A Physicochem.

Eng. Asp. 178 (1–3) (Mar. 2001) 187–198, https://doi.org/10.1016/S0927-7757(00)00705-6.

[51] J. Selsing, Internal Stresses in Ceramics, 419–419, J. Am. Ceram. Soc. 44 (8) (Aug. 1961), https://doi.org/10.1111/j.1151-2916.1961.tb15475.x.

[52] M. Carminati, M. Quarto, G. D'Urso, C. Giardini, G. Maccarini, Mechanical Characterization of AISI 316L Samples Printed Using Material Extrusion, Appl. Sci. 12 (3) (Jan. 2022) 1433, https://doi.org/10.3390/app12031433.

[53] N. Kurgan, R. Varol, Mechanical properties of P/M 316L stainless steel materials, Powder Technol. 201 (3) (Aug. 2010) 242–247, https://doi.org/10.1016/j.powtec.2010.03.041.

[54] A. Kasha, S.O. Obadimu, K.I. Kourousis, Flexural characteristics of material extrusion steel 316L: Influence of manufacturing parameters, Addit. Manuf. Lett. 3 (Dec. 2022) 100087, https://doi.org/10.1016/j.addlet.2022.100087.

[55] A.B.M. Supian, S.M. Sapuan, M.Y.M. Zuhri, E.S. Zainudin, H.H. Ya, Hybrid reinforced thermoset polymer composite in energy absorption tube application: A review, Def. Technol. 14 (Aug. 2018) 291–305, https://doi.org/10.1016/j.dt.2018.04.004.

[56] ISO 23317:2025, Implants for surgery – Materials – Simulated body fluid (SBF) preparation procedure and test method to detect apatite formation in SBF for initial screening of bone-contacting implant materials, International Organization for Standardization, Geneva, Switzerland, 2025.

[57] D. Bellucci, G. Bolelli, V. Cannillo, A. Cattini, A. Sola, situ Raman spectroscopy investigation of bioactive glass reactivity: simulated body fluid solution vs TRIS buffered solution, Mater. Charact. 62 (Oct. 2011) 1021–1028, https://doi.org/10.1016/j.matchar.2011.07.008.

[58] G. Penel, G. Leroy, C. Rey, E. Bres, MicroRaman spectral study of the PO4 and CO3 vibrational modes in synthetic and biological apatite, Calcif. Tissue Int. 63 (Dec. 1998) 475–481, https://doi.org/10.1007/s002239900561.

[59] A. Awonusi, M.D. Morris, M.M.J. Tecklenburg, Carbonate assignment and calibration in the Raman spectrum of apatite, Calcif. Tissue Int. 81 (Jul. 2007) 46–52, https://doi.org/10.1007/s00223-007-9034-0.

[60] L.L. Hench, The story of Bioglass®, J. Mater. Sci. Mater. Med. 17 (11) (Nov. 2006) 967–978, https://doi.org/10.1007/s10856-006-0432-z.

[61] D. Bellucci, V. Cannillo, A. Sola, F. Chiellini, M. Gazzarri, C. Migone, Macroporous Bioglass®-derived scaffolds for bone tissue regeneration, Ceram. Int. 37 (5) (Jul. 2011) 1575–1585, https://doi.org/10.1016/j.ceramint.2011.01.023.

[62] M.I. Alemany, P. Velasquez, M.A. de la Casa-Lillo, P.N. De Aza, Effect of materials' processing methods on the 'in vitro' bioactivity of wollastonite glass-ceramic materials, J. Non Cryst. Solids 351 (19–20) (Jul. 2005) 1716–1726, https://doi.org/10.1016/j.jnoncrysol.2005.04.062.

[63] R. Abd Rashid, R. Shamsudin, M.A. Abdul Hamid, A. Jalar, In-vitro bioactivity of wollastonite materials derived from limestone and silica sand, Ceram. Int. 40 (5) (Jun. 2014) 6847–6853, https://doi.org/10.1016/j.ceramint.2013.12.004.

[64] N.J. Hallab, S. Anderson, T. Stafford, T. Glant, J.J. Jacobs, Lymphocyte responses in patients with total hip arthroplasty, J. Orthop. Res. 23 (Mar. 2005) 384–391, https://doi.org/10.1016/j.orthres.2004.09.001.

[65] M. Geetha, A.K. Singh, R. Asokamani, A.K. Gogia, Ti based biomaterials, the ultimate choice for orthopaedic implants – A review, Progress. Mater. Sci. 54 (May 2009) 397–425, https://doi.org/10.1016/j.pmatsci.2008.06.004.

[66] Y. Lai, Ff Gao, Rt Ge, R. Liu, S. Ma, X. Liu, Metal ions overloading and cell death, Cell. Biol. Toxicol. 40 (Aug. 2024) 72, https://doi.org/10.1007/s10565-024-09910-4.